

A Spatial Concordance Correlation Coefficient with an Application to Image Analysis

Ronny Vallejos^{1*}, Javier Pérez², Aaron M. Ellison³ and Andrew D. Richardson⁴

^{1,2} Departamento de Matemática, Universidad Técnica Federico Santa María, Avenida España 1680, Valparaíso, Chile

³ Harvard Forest, Harvard University, Petersham, Massachusetts, USA

⁴ School of Informatics, Computing and Cyber Systems, Northern Arizona University, USA and Center for Ecosystem Science and Society, Northern Arizona University, USA

Abstract

In this work we define a spatial concordance coefficient for second-order stationary processes. This problem has been widely addressed in a non-spatial context, but here we consider a coefficient that for a fixed spatial lag allows one to compare two spatial sequences along a 45° line. The proposed coefficient was explored for the bivariate Matérn and Wendland covariance functions. The asymptotic normality of a sample version of the spatial concordance coefficient for an increasing domain sampling framework was established for the Wendland covariance function. To work with large digital images, we developed a local approach for estimating the concordance that uses local spatial models on non-overlapping windows. Monte Carlo simulations were used to gain additional insights into the asymptotic properties for finite sample sizes. As an illustrative example, we applied this methodology to two similar images of a deciduous forest canopy. The images were recorded with different cameras but similar fields-of-view and within minutes of each other. Our analysis showed that the local approach helped to explain a percentage of the non-spatial concordance and provided additional information about its decay as a function of the spatial lag.

Keywords: Bivariate Wendland covariance function; Concordance; Correlation; Lin's coefficient; Spatial correlation function.

1. Introduction

In recent decades, concordance correlation coefficients have been developed in a variety of different contexts. For instance, in assay or instrument validation processes, the reproducibility of the measurements among trials or laboratories is of interest. When a new instrument is developed, it may be relevant to evaluate whether its performance is concordant with other, existing ones, or its results accord with a “gold standard”. There are also situations in which one is interested in comparing two methods without a designated gold standard or target values (Lin et al., 2002). In the literature, this latter type of concordance has been tackled from different

*Corresponding author: R. Vallejos, ronny.vallejos@usm.cl

9 perspectives (Barnhart et al., 2007). Cohen (1968) discussed this problem in the context of
10 categorical data. Schall and Williams (1996) and Lin (2000) performed similar studies in the
11 context of bioequivalence.

12 One way to approach the concordance problem for continuous measurements is to construct
13 a scaled summary index that can take on values between -1 and 1 , analogous to a correlation
14 coefficient. Using this approach, Lin (1989) suggested a concordance correlation coefficient
15 (CCC) that evaluates the agreement between two continuous variables by measuring their joint
16 deviation from a 45° line through the origin. There have been some extensions of this CCC
17 that use several measuring instruments and techniques to evaluate the agreement between two
18 instruments; these efforts have led to interesting graphical tools (Hiriote and Chinchilli, 2011;
19 Stevens et al., 2017). In the context of goodness of fit, Vonesh et al. (1996) proposed a modified
20 Lin's CCC for choosing models that have a better agreement between the observed and the
21 predicted values. Recently Stevens et al. (2017) and Chodhary and Nagaraja (2017) developed
22 the probability of agreement, and Leal et al. (2019) studied the local influence of the CCC
23 and the probability of agreement considering both first- and second-order measures under the
24 case-weight perturbation scheme. Atkinson and Nevill (1997) critiqued the CCC because any
25 correlation coefficient is highly dependent on the measurement range. In general, therefore,
26 CCC is used only when measuring ranges are comparable or when methods are on the same
27 scale.

28 In this paper, we suggest an approach to assessing the agreement between two continuous
29 responses when the observations of both variables have been georeferenced in space. We define
30 a spatial CCC (SCCC) as a generalization of Lin's (1989) coefficient that measures the agree-
31 ment between two spatial variables. For a fixed lag, our SCCC shares the same properties as
32 the original CCC. For an increasing domain sampling scheme, (i.e., for an asymptotic method
33 for which the two-dimensional domain increases), we establish the asymptotic normality of
34 the sample SCCC for a bivariate Gaussian process with a Wendland covariance function. To
35 facilitate the computation of the spatial concordance coefficient when image sizes are large, we
36 developed a local approach for estimating it that uses local spatial models on non-overlapping
37 windows. This approach constitutes a new way of thinking about concordance that has not
38 been considered previously, especially for large digital images. Our approach also captures the
39 decay of the SCCC as a function of the norm of the spatial lag. Monte Carlo simulations and
40 numerical experiments with real datasets accompany the exposition of the methodological as-
41 pects. An image-analysis example is worked in detail to illustrate the fitting of a local SCCCs.
42 We conclude with a summary of the main findings and an outline of problems to be tackled in
43 future research.

44 2. Preliminaries and Notation

Assume that X and Y are two continuous random variables such that the joint distribution
of X and Y has finite second moments with means μ_X and μ_Y , variances σ_X^2 and σ_Y^2 , covariance
 σ_{XY} and correlation coefficient between X and Y

$$\rho = \frac{\sigma_{XY}}{\sigma_X \sigma_Y}.$$

The mean squared deviation of $D = X - Y$ is

$$\text{MSD} = \varepsilon^2 = \mathbb{E}[D^2] = \mathbb{E}[(X - Y)^2].$$

It is straightforward to see that $\varepsilon^2 = (\mu_X - \mu_Y)^2 + \sigma_X^2 + \sigma_Y^2 - 2\sigma_{XY}$ and the sample counterpart satisfies $e^2 = (\bar{X} - \bar{Y})^2 + s_X^2 + s_Y^2 - 2s_{XY}$. Using this framework, Lin (1989) defined a CCC as:

$$\rho_c = 1 - \frac{\varepsilon^2}{\varepsilon^2|\rho|} = \frac{2\sigma_{XY}}{\sigma_X^2 + \sigma_Y^2 + (\mu_X - \mu_Y)^2}, \quad (1)$$

where $\varepsilon^2|\rho| = 0$ is the error, given that the correlation coefficient between X and Y is null. Lin (1989) pointed out that Equation (1) is equal to one minus the ratio between the expected squared perpendicular deviation from the 45° -line intersecting the origin, and the expected squared perpendicular deviation from it when X and Y are uncorrelated.

The CCC satisfies the following properties:

1. $\rho_c = \alpha \cdot \rho$, where $\alpha = \frac{2}{w+1/w+\nu^2}$, $\nu = \frac{\mu_X - \mu_Y}{\sqrt{\sigma_X \sigma_Y}}$, and $w = \frac{\sigma_X}{\sigma_Y}$.
2. $|\rho_c| \leq |\rho| \leq 1$.
3. $\rho_c = 0$ if and only if $\rho = 0$.
4. $\rho_c = \rho$ if and only if $\sigma_Y = \sigma_X$ and $\mu_Y = \mu_X$.

It should be emphasized that ρ_c is always less than ρ because the first coefficient evaluates the degree to which pairs fall on the 45° -line intersecting the origin, but it is not the exact linear correlation between X and Y .

The sample estimate of ρ_c is given as:

$$\hat{\rho}_c = \frac{2s_{XY}}{s_X^2 + s_Y^2 + (\bar{X} - \bar{Y})^2}.$$

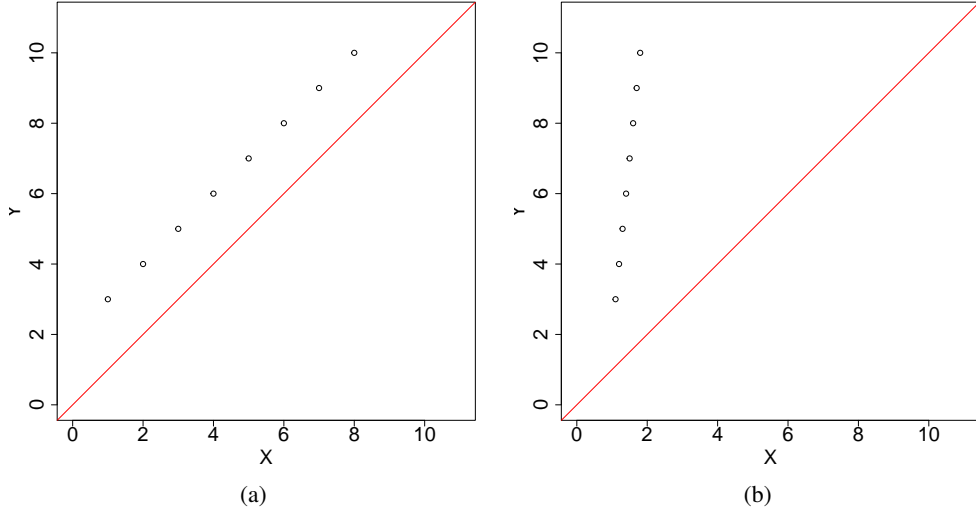


Figure 1: Departure of two datasets defined on the plane from the 45° line intersecting the origin. (a) Perfect correlation with a shift effect results in relatively high concordance ($\hat{\rho}_c = 0.7241$). (b) Perfect correlation but poor concordance ($\hat{\rho}_c = 0.0340$).

To clarify the difference between the CCC and the correlation coefficient, two examples are illustrated in Figure 1. Figure 1 (a) is a scatterplot for the case where there are different sample means but identical sample variances ($X = (1, 2, 3, \dots, 8), Y = (3, 4, 5, \dots, 10)$); the correlation between X and Y coefficient is equal to 1 and $\hat{\rho}_c = 0.7241$. Figure 1 (b) illustrates the case where both sample means and variances differ ($X = (1.1, 1.2, 1.3, \dots, 1.8), Y = (3, 4, 5, \dots, 10)$). As in Figure 1 (a), there is a perfect correlation between X and Y ($\hat{\rho} = 1$), but now there is much lower concordance X and Y ($\hat{\rho}_c = 0.0340$).

Inference for this coefficient was addressed via Fisher's transformation. Lin (1989) proved that

$$\hat{Z} = \frac{1}{2} \log \left(\frac{1 + \hat{\rho}_c}{1 - \hat{\rho}_c} \right) \xrightarrow{\mathcal{D}} \mathcal{N}(Z, \sigma_Z^2), \text{ as } n \rightarrow \infty,$$

where

$$Z = \tanh^{-1}(\rho_c) = \frac{1}{2} \log \left(\frac{1 + \rho_c}{1 - \rho_c} \right)$$

and

$$\sigma_Z^2 = \frac{1}{n-2} \left[\frac{(1-\rho^2)\rho_c^2}{(1-\rho_c^2)\rho^2} + \frac{4\rho^2(1-\rho_c)\rho_c^3}{(1-\rho_c^2)^2\rho} + \frac{2\rho^4\rho_c^4}{(1-\rho_c^2)^2\rho^2} \right].$$

As a consequence of the asymptotic normality of the sample CCC, an approximate hypothesis testing problem of the form

$$H_0 : \rho_c = \rho_0 \text{ versus } H_1 : \rho_c \neq \rho_0$$

for a fixed ρ_0 can be constructed. Alternatively, an approximate confidence interval for ρ_c of the form

$$[\tanh(Z - z_{\alpha/2}\sigma_Z), \tanh(Z + z_{\alpha/2}\sigma_Z)]$$

65 can be used, where $z_{\alpha/2}$ is the upper quantile of order $\alpha/2$ of the standard normal distribution.
 66 Applications and extensions of Lin's coefficient can be found in [Lin et al. \(2012\)](#), among others.

67 Although the notion of concordance and particularly Lin's coefficient have been general-
 68 ized to different contexts, they also have been criticized. [Atkinson and Nevill \(1997\)](#) questioned
 69 Lin's coefficient for two reasons. First, these kind of methods are highly sensitive to sample
 70 heterogeneity. Second, its interpretation is problematic, especially when ρ_c is small. [Lawrence](#)
 71 and [Chinchilli \(1997\)](#) argued that most of the correlation coefficients largely depend on the an-
 72 alytical range, so that good concordance observed over a small range of measurements cannot
 73 be extrapolated to a similarly good concordance over a larger range of measurements. Three
 74 factors contribute to low values of ρ_c : small analytical range, imprecision, and inaccuracy (sys-
 75 tematic bias) ([Lawrence and Chinchilli, 1997](#)). Because of these factors, study design plays a
 76 crucial role in the interpretation of Lin's coefficient. Measurement ranges should be compatible
 77 and they should be reported together with Lin's coefficient.

78 3. A Spatial Concordance Coefficient and its Properties

79 In this section we generalize Lin's coefficient for bivariate spatial processes. The main
 80 advantage of this extension is the fact that the new coefficient considers the existing spatial
 81 information of a georeferenced sample on the two-dimensional space. The way the coefficient
 82 takes into account the spatial association is through its dependence on a spatial lag $\mathbf{h} \in \mathbb{R}^2$,
 83 similarly to the covariance function or the variogram of a weakly stationary process. This ex-
 84 tension preserves Lin's interpretation in the sense that for a particular spatial lag, the spatial
 85 concordance captures the departure from the 45° line passing through the origin. In particular,
 86 for isotropic processes the aim of this extension is to yield a plot of the spatial concordance co-
 87 efficient versus the norm of the spatial lag. This will help to study the decay of the concordance
 88 as a function of the distance between the observations.

89 We start by extending Lin's CCC for bivariate second-order spatial processes for a general
 90 bivariate covariance function and a fixed lag in space.

Definition 1. Let $\mathbf{Z}(\mathbf{s}) = (X(\mathbf{s}), Y(\mathbf{s}))^\top$ be a bivariate second-order stationary random field
 with $\mathbf{s}, \mathbf{h} \in \mathbb{R}^2$, mean $(\mu_X, \mu_Y)^\top$, and covariance function

$$C(\mathbf{h}) = \begin{pmatrix} C_X(\mathbf{h}) & C_{XY}(\mathbf{h}) \\ C_{YX}(\mathbf{h}) & C_Y(\mathbf{h}) \end{pmatrix},$$

where

$$\begin{aligned} C_X(\mathbf{h}) &= \text{Cov}[X(\mathbf{s}), X(\mathbf{s} + \mathbf{h})], \\ C_Y(\mathbf{h}) &= \text{Cov}[Y(\mathbf{s}), Y(\mathbf{s} + \mathbf{h})], \\ C_{XY}(\mathbf{h}) &= C_{YX}(\mathbf{h}) = \text{Cov}[X(\mathbf{s}), Y(\mathbf{s} + \mathbf{h})]. \end{aligned}$$

Then the SCCC is defined as

$$\begin{aligned} \rho^c(\mathbf{h}) &= 1 - \frac{\mathbb{E}[(X(\mathbf{s} + \mathbf{h}) - Y(\mathbf{s}))^2]}{\mathbb{E}[(X(\mathbf{s} + \mathbf{h}) - Y(\mathbf{s}))^2 | C_{XY}(\mathbf{0}) = 0]} \\ &= \frac{2C_{XY}(\mathbf{h})}{C_X(\mathbf{0}) + C_Y(\mathbf{0}) + (\mu_X - \mu_Y)^2}. \end{aligned} \tag{2}$$

Some straightforward properties of this SCCC are:

1. For $\eta = \frac{2\sqrt{C_X(\mathbf{0})C_Y(\mathbf{0})}}{C_X(\mathbf{0})+C_Y(\mathbf{0})+(\mu_X-\mu_Y)^2}$, and $\rho_{XY}(\mathbf{h}) = \frac{C_{XY}(\mathbf{h})}{\sqrt{C_X(\mathbf{0})C_Y(\mathbf{0})}}$, it follows that

$$\rho^c(\mathbf{h}) = \eta \cdot \rho_{YX}(\mathbf{h}). \quad (3)$$

2. $|\rho^c(\mathbf{h})| \leq |\rho_{XY}(\mathbf{h})| \leq 1$.
 3. $\rho^c(\mathbf{h}) = 0$ iff $\rho_{XY}(\mathbf{h}) = 0$.
 4. $\rho^c(\mathbf{h}) = \rho_{XY}(\mathbf{h})$ iff $\mu_X = \mu_Y$ and $C_X(\mathbf{0}) = C_Y(\mathbf{0})$.

In the sequel, the estimation of parametric covariance functions will be relevant, so we first define them for parametric correlations. If $R(\mathbf{h}, \phi)$ is a correlation function with parameter vector ϕ , then a covariance function is defined as:

$$\begin{aligned} C_X(\mathbf{h}) &= \sigma_X^2 R(\mathbf{h}, \phi_X), \\ C_Y(\mathbf{h}) &= \sigma_Y^2 R(\mathbf{h}, \phi_Y), \\ C_{XY}(\mathbf{h}) &= \rho_{XY} \sigma_X \sigma_Y R(\mathbf{h}, \phi_{XY}). \end{aligned} \quad (4)$$

The SCCC then can be written as:

$$\rho^c(\mathbf{h}) = \frac{2\sigma_X \sigma_Y}{\sigma_X^2 + \sigma_Y^2} \rho_{XY} R(\mathbf{h}, \phi_{XY}). \quad (5)$$

This means that the SCCC can be seen as a corrected version of the correlation between processes $X(\cdot)$ and $Y(\cdot)$. Because we expect that $\rho^c(|\mathbf{h}|)$ in general will decrease as a function of $|\mathbf{h}|$, it is possible to quantify the relationship between the spatial concordance and Lin's coefficient for a fixed spatial lag. Moreover, the value of $|\mathbf{h}|$ for which $\rho^c(|\mathbf{h}|)$ is negligible when it decreases as a function of $|\mathbf{h}|$ can be quantified similarly to the correlation function. In this case, the range of SCCC is the value of the norm of \mathbf{h} for which $\rho^c(|\mathbf{h}|)$ is zero.

Using similar arguments as in properties 1–4, the SCCC in (5) could be derived for specific parametric bivariate correlation functions. Here we provide two examples.

1. For a bivariate random field with mean $(\mu, \mu)^\top$ and the Matérn covariance function

$$C_X(\mathbf{h}) = \sigma_X^2 M(\mathbf{h}, v_X, a_X), \quad (6)$$

$$C_Y(\mathbf{h}) = \sigma_Y^2 M(\mathbf{h}, v_Y, a_Y), \quad (7)$$

$$C_{XY}(\mathbf{h}) = \rho_{XY} \sigma_X \sigma_Y M(\mathbf{h}, v_{XY}, a_{XY}), \quad (8)$$

where $M(\mathbf{h}, v, a) = (a|\mathbf{h}|)^v K_v(a|\mathbf{h}|)$, $K_v(\cdot)$ is a modified Bessel function of the second kind, $\|\cdot\|$ is the Euclidean norm in \mathbb{R}^2 , and ρ_{XY} is the co-located correlation coefficient

between X and Y (defined by Gneiting et al., 2010). It follows that

$$\begin{aligned}
\rho^c(\mathbf{h}) &= \frac{2C_{XY}(\mathbf{h})}{C_X(\mathbf{0}) + C_Y(\mathbf{0}) + (\mu - \mu)^2} \\
&= \frac{2\rho_{XY}\sigma_X\sigma_Y M(\mathbf{h}, v_{XY}, a_{XY})}{\sigma_X^2 M(\mathbf{0}, v_X, a_X) + \sigma_Y^2 M(\mathbf{0}, v_Y, a_Y)} \\
&= \frac{2\rho_{XY}\sigma_X\sigma_Y M(\mathbf{h}, v_{XY}, a_{XY})}{\sigma_X^2 + \sigma_Y^2} \\
&= \frac{2\sigma_X\sigma_Y M(\mathbf{h}, v_{XY}, a_{XY})}{\sigma_X^2 + \sigma_Y^2} \cdot \rho_{XY} \\
&= \eta(\mathbf{h}) \cdot \rho_{XY},
\end{aligned}$$

103 where $\eta(\mathbf{h}) = \frac{2\sigma_X\sigma_Y M(\mathbf{h}, v_{XY}, a_{XY})}{\sigma_X^2 + \sigma_Y^2}$.

A special case of the Matérn covariance function is when $v_{XY} = p + 1/2$. Then

$$M(\mathbf{h}, v_{XY}, a_{XY}) = M(\mathbf{h}, p + 1/2, a_{XY}) = \exp(-a_{XY}\|\mathbf{h}\|) \sum_{k=0}^p \frac{(p+k)!}{(2p)!} \binom{p}{k} (2a_{XY}\|\mathbf{h}\|)^{p-k},$$

and the SCCC is

$$\rho^c(\mathbf{h}) = \frac{2\sigma_{XY}}{\sigma_X^2 + \sigma_Y^2} \exp(-a_{XY}\|\mathbf{h}\|) \sum_{k=0}^p \frac{(p+k)!}{(2p)!} \binom{p}{k} (2a_{XY}\|\mathbf{h}\|)^{p-k}.$$

By choosing $p = 0$ and $M(\mathbf{h}, 1/2, a_{XY}) = \exp(-a_{XY}\|\mathbf{h}\|)$, the SCCC can be written in its simplest form:

$$\rho^c(\mathbf{h}) = \frac{2\sigma_{XY}}{\sigma_X^2 + \sigma_Y^2} \exp(-a_{XY}\|\mathbf{h}\|).$$

104 For illustrative purposes, consider $\sigma_X = 1$, $\sigma_Y = 2$, $\sigma_{XY} = 1.8$, $a_{XY} = 1/2$ and $v = v_{XY} =$
105 $\{\frac{1}{2}, \frac{3}{2}, \frac{5}{2}\}$. Then for $\|\mathbf{h}\| \in \{0, 1, \dots, 15\}$, the SCCCs for different values of the smoothing
106 parameter v and using the Matérn covariance function are illustrated in Figure 2. The
107 curves of the SCCC decay more rapidly to zero as v increases.

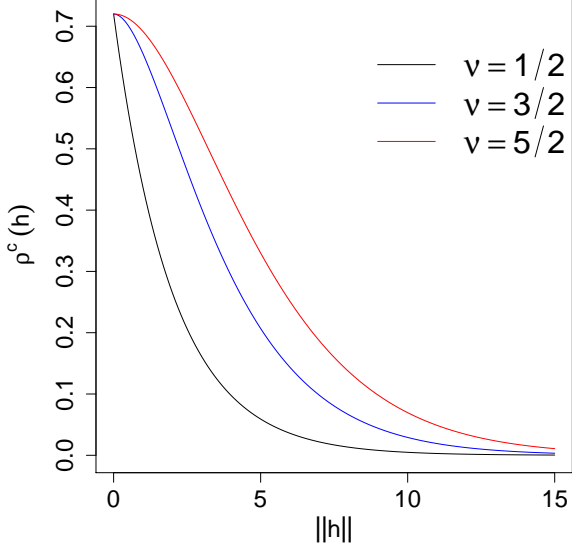


Figure 2: $\rho^c(\mathbf{h})$ versus $\|\mathbf{h}\|$ for the Matérn covariance function and different values of the smoothness parameter v .

2. For a bivariate Wendland-Gneiting covariance function (Daley et al., 2015) of the form

$$\begin{aligned} C_X(\mathbf{h}) &= \sigma_X^2 W(\mathbf{h}, b_X, \gamma_X), \\ C_Y(\mathbf{h}) &= \sigma_Y^2 W(\mathbf{h}, b_Y, \gamma_Y), \\ C_{XY}(\mathbf{h}) &= \rho_{XY} \sigma_X \sigma_Y W(\mathbf{h}, b_{XY}, \gamma_{XY}), \end{aligned} \quad (9)$$

where

$$W(\mathbf{h}, b, \gamma) = b^{\gamma+2k+1} B(\gamma+2k+1, \gamma+1) \tilde{\Psi}_{\gamma+1, k} \left(\frac{\|\mathbf{h}\|}{b} \right),$$

$B(\cdot, \cdot)$ is the beta function, and $\tilde{\Psi}_{\gamma, k}$ is defined for $k \geq 1$ as

$$\tilde{\Psi}_{\gamma, k}(t) = \int_t^1 \frac{u(u^2 - t^2)^{k-1} (1-u)_+^\gamma}{B(2k, \gamma+1)} du, \quad 0 \leq t \leq 1,$$

where $(x)_+ = \mathbf{1}_{(x \geq 0)}$ (Gneiting, 2002), the SCCC is

$$\rho^c(\mathbf{h}) = \frac{2\rho_{XY} \sigma_X \sigma_Y W(\mathbf{h}, b_{XY}, \gamma_{XY})}{\sigma_X^2 + \sigma_Y^2 + (\mu_X - \mu_Y)^2}, \quad \mathbf{h} \in \mathbb{R}^2.$$

In particular, considering $W(\mathbf{h}, b_{XY}, \gamma_{XY}) = p_k(\|\mathbf{h}\|)(1 - \|\mathbf{h}\|/b_{XY})_+^l$, where $k = 1$, $l = \gamma + 1$, $\gamma = 0$ and $b_{XY} > 0$,

$$\rho^c(\mathbf{h}) = \frac{2\rho_{XY} \sigma_X \sigma_Y (1 + l\|\mathbf{h}\|/b_{XY}) (1 - \|\mathbf{h}\|/b_{XY})_+^l}{\sigma_X^2 + \sigma_Y^2 + (\mu_X - \mu_Y)^2}. \quad (10)$$

¹⁰⁸ **4. Inference**

¹⁰⁹ In the previous section we showed that for several covariance structures, the spatial con-
¹¹⁰ cordance correlation coefficient defined in equation (2) can be written as a product of the cor-
¹¹¹ relation function and a constant. Thus, we can consider plug-in estimators for the correlation
¹¹² function and the constant.

¹¹³ Let $Z(s) = (X(s), Y(s))^\top$, $s \in D \subset \mathbb{R}^2$ be a Gaussian process with mean $\mu = (\mu_X, \mu_Y)^\top$ and covariance function $C(\mathbf{h})$, $s, \mathbf{h} \in \mathbb{R}^2$. Then a sample (plug-in) estimate of the SCCC index (3) is

$$\hat{\rho}^c(\mathbf{h}) = \hat{\eta} \cdot \hat{\rho}_{XY}(\mathbf{h}), \quad (11)$$

¹¹⁴ where $\hat{\eta} = ((\hat{a} + 1/\hat{a} + \hat{b}^2)/2)^{-1}$, $\hat{a} = \left(\frac{\hat{C}_{XX}(\mathbf{0})}{\hat{C}_{YY}(\mathbf{0})} \right)^{1/2}$, $\hat{b} = \frac{\hat{\mu}_X - \hat{\mu}_Y}{(\hat{C}_{XX}(\mathbf{0})\hat{C}_{YY}(\mathbf{0}))^{1/4}}$, and $\hat{\mu}_X$, $\hat{\mu}_Y$, $\hat{C}_{XX}(\mathbf{0})$, and $\hat{C}_{YY}(\mathbf{0})$ are the maximum likelihood (ML) estimates of μ_X , μ_Y , $C_{XX}(\mathbf{0})$, and $C_{YY}(\mathbf{0})$, respectively.

¹¹⁵ The asymptotic properties of an estimator like equation (11) have been studied in the literature for specific cases. [Bevilacqua et al. \(2015\)](#) studied the asymptotic properties of the ML estimator for a separable Matérn covariance model. They used a result provided by [Mardia and Marshall \(1984\)](#) in an increasing domain sampling framework: a process $Z(s)$, with points s_1, \dots, s_n located in a rectangle $D_n \subset \Delta \mathbb{Z}^2$, for $0 < \Delta < \infty$, such that D_n satisfies the increasing condition $D_n \subset D_{n+1}$, for all n .

¹¹⁶ Using this theorem and the delta method, we can establish the following result for the
¹¹⁷ Wendland-Gneiting model:

Theorem 1. Let $Z(s)$, $s \in D \subset \mathbb{R}^2$ be a bivariate Gaussian spatial process with mean $\mathbf{0}$ and covariance function given by

$$\begin{aligned} C_X(\mathbf{h}) &= \sigma_X^2 \left(1 + (\nu + 1) \frac{\|\mathbf{h}\|}{b_X} \right) \left(1 - \frac{\|\mathbf{h}\|}{b_X} \right)_+^{\nu+1}, \\ C_Y(\mathbf{h}) &= \sigma_Y^2 \left(1 + (\nu + 1) \frac{\|\mathbf{h}\|}{b_Y} \right) \left(1 - \frac{\|\mathbf{h}\|}{b_Y} \right)_+^{\nu+1}, \\ C_{XY}(\mathbf{h}) = C_{YX}(\mathbf{h}) &= \rho_{XY} \sigma_X \sigma_Y \left(1 + (\nu + 1) \frac{\|\mathbf{h}\|}{b_{XY}} \right) \left(1 - \frac{\|\mathbf{h}\|}{b_{XY}} \right)_+^{\nu+1}, \end{aligned}$$

for $\nu > 0$ fixed. Define $\boldsymbol{\theta} = (\sigma_X^2, \sigma_Y^2, \rho_{XY}, b_{XY})^\top$ and denote the ML estimator of $\boldsymbol{\theta}$ as $\hat{\boldsymbol{\theta}}_n$. Then,

$$\left(\nabla g(\boldsymbol{\theta})^\top \mathbf{F}_n(\boldsymbol{\theta})^{-1} \nabla g(\boldsymbol{\theta}) \right)^{-1/2} (g(\hat{\boldsymbol{\theta}}_n) - g(\boldsymbol{\theta})) \xrightarrow{D} \mathcal{N}(0, 1), \text{ as } n \rightarrow \infty,$$

in an increasing domain sense, where

$$g(\boldsymbol{\theta}) = \frac{2\rho_{XY}\sigma_X\sigma_Y \left(1 + (\nu + 1) \frac{\|\mathbf{h}\|}{b_{XY}} \right) \left(1 - \frac{\|\mathbf{h}\|}{b_{XY}} \right)_+^{\nu+1}}{\sigma_X^2 + \sigma_Y^2},$$

$\mathbf{F}_n(\boldsymbol{\theta})^{-1}$ is the Fisher information matrix with respect to $\boldsymbol{\beta}$ and $\boldsymbol{\theta}_n$,

$$\nabla g(\boldsymbol{\theta}) = \begin{pmatrix} \frac{\sigma_Y \rho_{XY} (\sigma_Y^2 - \sigma_X^2) \left(1 + (v+1) \frac{\|\mathbf{h}\|}{b_{XY}}\right) \left(1 - \frac{\|\mathbf{h}\|}{b_{XY}}\right)_+^{v+1}}{\sigma_X (\sigma_X^2 + \sigma_Y^2)^2} \\ \frac{\sigma_X \rho_{XY} (\sigma_X^2 - \sigma_Y^2) \left(1 + (v+1) \frac{\|\mathbf{h}\|}{b_{XY}}\right) \left(1 - \frac{\|\mathbf{h}\|}{b_{XY}}\right)_+^{v+1}}{\sigma_Y (\sigma_X^2 + \sigma_Y^2)^2} \\ \frac{2\sigma_X \sigma_Y \left(1 + (v+1) \frac{\|\mathbf{h}\|}{b_{XY}}\right) \left(1 - \frac{\|\mathbf{h}\|}{b_{XY}}\right)_+^{v+1}}{\sigma_X^2 + \sigma_Y^2} \\ \frac{2\sigma_X \sigma_Y \rho_{XY} f(b_{XY})}{\sigma_X^2 + \sigma_Y^2} \end{pmatrix},$$

124 and $f(b_{XY}) = \left(-\frac{(v+1)\|\mathbf{h}\|}{b_{XY}^2}\right) \left(1 - \frac{\|\mathbf{h}\|}{b_{XY}}\right)_+^{v+1} + \left(1 + \frac{(v+1)\|\mathbf{h}\|}{b_{XY}}\right) \left(1 - \frac{\|\mathbf{h}\|}{b_{XY}}\right)_+^v \frac{(v+1)\|\mathbf{h}\|}{b_{XY}^2}$.

125 *Proof.* See the Appendix. □

126 5. A Local Approach

127 When the sizes of the images for which correspondence is to be assessed are large, it can
128 be difficult to find a single model fitting reasonably well to the entire image(s). This has been
129 investigated in the literature for autoregressive processes defined on the plane in the context of
130 image restoration and segmentation (for examples, see [Bustos et al., 2009](#)).

Here we describe a local approach for a bivariate process of the form $\mathbf{Z}(s)$, $s \in D \subset \mathbb{R}^2$, where the observations are located over a rectangular grid of size $n \times m$. The extension to an $l \in \mathbb{N}$ -variate process is natural when $l > 2$. In this framework, we assume that the whole domain D can be divided into p sub-windows D_i , such that $\cup_{i=1}^p D_i = D$, for $i = 1, \dots, p$. Then we define p processes of the form $\mathbf{Z}_i(s) = (\mathbf{X}_i(s), \mathbf{Y}_i(s))^\top$, $s \in D_i$, where each process has a covariance function given by

$$\begin{aligned} C_{X,i}(\mathbf{h}) &= \sigma_{X,i}^2 R(\mathbf{h}, \phi_{X,i}), \\ C_{Y,i}(\mathbf{h}) &= \sigma_{Y,i}^2 R(\mathbf{h}, \phi_{Y,i}), \\ C_{XY,i}(\mathbf{h}) &= \rho_{XY,i} \sigma_{X,i} \sigma_{Y,i} R(\mathbf{h}, \phi_{XY,i}), \quad i = 1, \dots, p, \end{aligned} \tag{12}$$

where $R(\mathbf{h}, \phi)$ is a correlation function with parameter vector ϕ , and $\mathbf{Z}_i(\cdot)$ and $\mathbf{Z}_j(\cdot)$ are supposed to be independent ([Ojeda et al., 2010](#)). Then for each local process $\mathbf{Z}_i(\cdot)$ we define the local SCCC $\rho_i^c(\cdot)$ using the theory developed in Section 3:

$$\rho_i^c(\mathbf{h}) = \frac{2\sigma_{X,i} \sigma_{Y,i}}{\sigma_{X,i}^2 + \sigma_{Y,i}^2} \rho_{XY,i} R(\mathbf{h}, \phi_{XY,i}). \tag{13}$$

Based on the local coefficients $\rho_i^c(\cdot)$, we suggest two global SCCCs. The first one is the average of the p local coefficients:

$$\rho_1(\mathbf{h}) = \frac{1}{p} \sum_{i=1}^p \rho_i^c(\mathbf{h}). \tag{14}$$

¹³¹ The second one considers the average of each parameter in the correlation function such that
¹³² the global coefficient is

$$\rho_2(\mathbf{h}) = \frac{2\bar{\sigma}_X\bar{\sigma}_Y}{\bar{\sigma}_X^2 + \bar{\sigma}_Y^2} \bar{\rho}_{XY} R(\mathbf{h}, \bar{\phi}_{XY}), \quad (15)$$

¹³³ $\bar{\sigma}_X = \frac{1}{p} \sum_{i=1}^p \sigma_{X,i}$, and similarly for $\bar{\sigma}_Y$, $\bar{\rho}_{XY}$, and $R(\mathbf{h}, \bar{\phi}_{XY})$. As a result, we have two global
¹³⁴ coefficients of spatial concordance depending on averages: the first one is the average of the local coefficients and the second one is a plug-in of the parameter averages.

When process $Z(s)$ have been observed in the sites s_1, \dots, s_n and all the local coefficients have been computed, the sample versions of $\rho_1(\cdot)$ and $\rho_2(\cdot)$ are

$$\begin{aligned}\hat{\rho}_1(\mathbf{h}) &= \frac{1}{p} \sum_{i=1}^p \hat{\rho}_i^c(\mathbf{h}), \\ \hat{\rho}_2(\mathbf{h}) &= \frac{2\hat{\bar{\sigma}}_X\hat{\bar{\sigma}}_Y}{\hat{\bar{\sigma}}_X^2 + \hat{\bar{\sigma}}_Y^2} \hat{\bar{\rho}}_{XY} R(\mathbf{h}, \hat{\bar{\phi}}_{XY}),\end{aligned}$$

¹³⁶ where $\hat{\bar{\sigma}}_X$, $\hat{\bar{\sigma}}_Y$, $\hat{\bar{\rho}}_{XY}$, and $R(\mathbf{h}, \hat{\bar{\phi}}_{XY})$ are the means of the ML estimators of the parameters defined in equation (15).

Considering an increasing domain sampling scheme, the asymptotic normality of $\hat{\rho}_1(\mathbf{h})$ is straightforward. Indeed, let $Z_i(s) = (X_i(s), Y_i(s))^\top$, $s \in D_i$, be a bivariate process with correlation structure given by (12). Define the parameter vector $\boldsymbol{\theta}^i = (\rho_{XY,i}, \sigma_{X,i}, \sigma_{Y,i}, \sigma_{XY,i}, \phi_{XY,i})^\top$ associated with $Z_i(s)$ and denote the ML estimator of $\boldsymbol{\theta}^i$ as $\hat{\boldsymbol{\theta}}_n^i$. If the covariance satisfies the Mardia and Marshall (1984) conditions, then

$$\hat{\boldsymbol{\theta}}_n^i \xrightarrow{D} \mathcal{N}(\boldsymbol{\theta}^i, \mathbf{F}_n^i(\boldsymbol{\theta}^i)^{-1}),$$

where $\mathbf{F}_n^i(\boldsymbol{\theta}^i)$ is the covariance matrix of $\hat{\boldsymbol{\theta}}_n^i$. Then for $g(\boldsymbol{\theta}) = \rho_i^c(\mathbf{h})$,

$$\left(\nabla g(\boldsymbol{\theta}^i)^\top \mathbf{F}_n^i(\boldsymbol{\theta}^i)^{-1} \nabla g(\boldsymbol{\theta}^i) \right)^{-1/2} (g(\hat{\boldsymbol{\theta}}_n^i) - g(\boldsymbol{\theta}^i)) \xrightarrow{D} \mathcal{N}(\mathbf{0}, 1).$$

Assuming that $Z_i(s)$ and $Z_j(s)$ are independent for all $i \neq j$,

$$\hat{\rho}_1(\mathbf{h}) = \frac{1}{p} \sum_{i=1}^p \hat{\rho}_i^c(\mathbf{h}) \xrightarrow{D} \mathcal{N} \left(\rho_i^c(\mathbf{h}), \frac{1}{p^2} \sum_{i=1}^p \nabla g(\boldsymbol{\theta}^i)^\top \mathbf{F}_n^i(\boldsymbol{\theta}^i)^{-1} \nabla g(\boldsymbol{\theta}^i) \right).$$

¹³⁸ 6. Monte Carlo Simulations

¹³⁹ We used Monte Carlo simulations to explore the properties of the SCCC, $\rho^c(\cdot)$, for finite
¹⁴⁰ samples sizes. The performance of the ML estimates were then analyzed with respect to the true
¹⁴¹ values of the coefficient. We generated 500 replicates from a Gaussian random field sampled
¹⁴² on a regular lattice of size 20×20 inside the region $[-\frac{3}{2}, \frac{3}{2}]^2$. Each replicate was generated from
¹⁴³ a bivariate Gaussian random field with mean zero and Wendland-Gneiting covariance function
¹⁴⁴ given in equation (9). In each case, we estimated the parameters of the covariance function
¹⁴⁵ using ML and used them to compute the SCCC given in equation (10). Four set of parameters
¹⁴⁶ were considered to assess the performance of the SCCC when these parameters vary:

- 147 1. Case 1: $\sigma_X = \sigma_Y = 1$, $\rho_{XY} = -0.15$, $b_X = 0.5$, $b_Y = 0.4$, $b_{XY} = 0.35$.
 148 2. Case 2: $\sigma_X = \sigma_Y = 1$, $\rho_{XY} = 0.25$, $b_X = 1.2$, $b_Y = 0.9$, $b_{XY} = 1$.
 149 3. Case 3: $\sigma_X = \sigma_Y = 1$, $\rho_{XY} = 0.3$, $b_X = 1.8$, $b_Y = 1.4$, $b_{XY} = 1.5$.
 150 4. Case 4: $\sigma_X = 2$, $\sigma_Y = 0.5$, $\rho_{XY} = 0.45$, $b_X = 1.1$, $b_Y = 1$, $b_{XY} = 0.9$.

151 Note that in all cases $v = 4$ and $k = 1$ and that Case 4 includes different marginal variances.
 152 In Figure 3 we show a realization of the random field for each case.

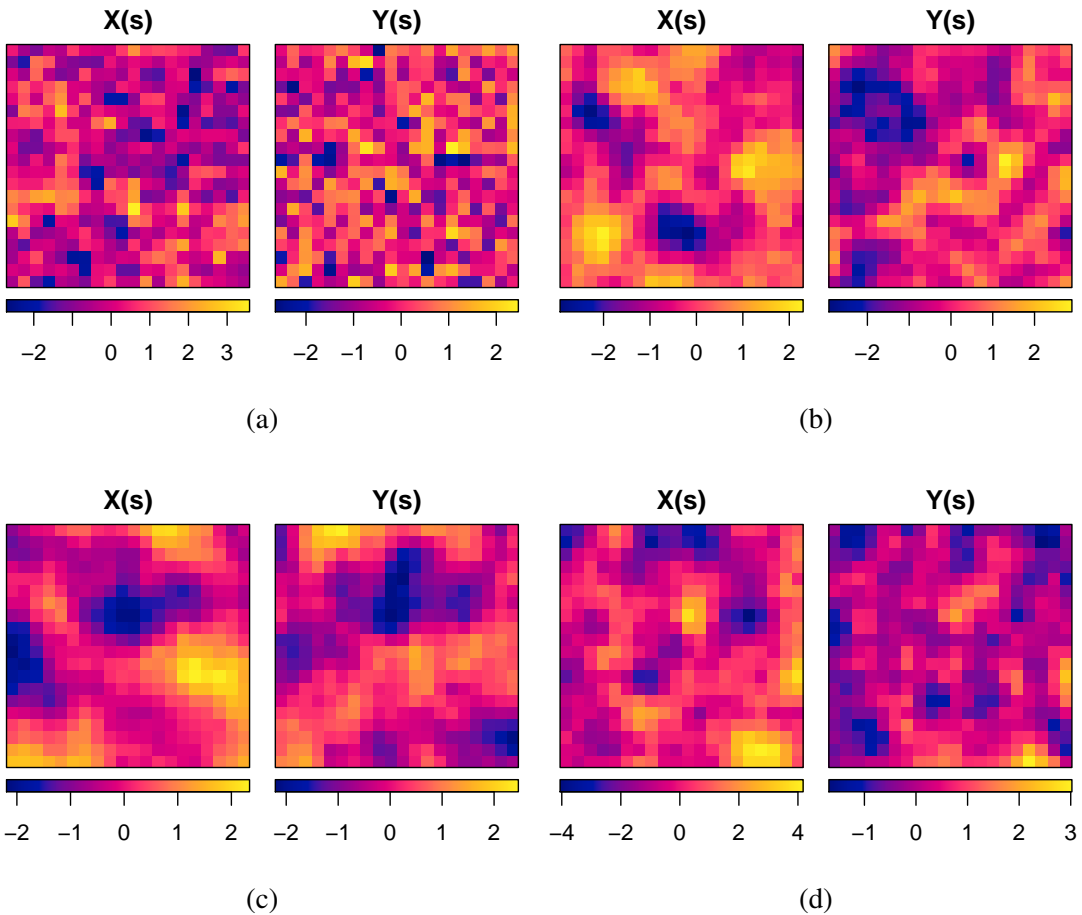


Figure 3: Realization of a Gaussian random field with bivariate Wendland-Gneiting correlation function. (a) Case 1; (b) Case 2; (c) Case 3; (d) Case 4.

153 Table 1 summarizes the estimates of the Wendland-Gneiting model for the simulations.
 154 The estimates were obtained using ML estimation and the values reported are the average over
 155 500 simulation runs. In each case the value of the standard error is in parenthesis under the
 156 estimation. In general we observed reasonable estimates of all parameters and small standard
 157 errors.

158 The ML estimates of the parameters of the Wendland-Gneiting covariance function had low
 159 bias and standard errors, and agreed with previously published results (e.g., [Bevilacqua et al.](#),

¹⁶⁰ 2019). Using these estimates, we computed the SCCC in each case for $0 < \|\mathbf{h}\| < 2$. This
¹⁶¹ length for $\|\mathbf{h}\|$ was enough to observe the decay of the SCCC in each case even though the
¹⁶² maximum distance between two points in the region was $3\sqrt{2}$ (Figure 4).

¹⁶³ The mean square errors of the estimates shown in (Table 1) were all less than $1.6485 \cdot 10^{-6}$,
¹⁶⁴ 0.0001, $6.5292 \cdot 10^{-5}$, and $9.3775 \cdot 10^{-6}$, respectively, for cases 1–4. $\rho^c(\mathbf{h})$ versus $\|\mathbf{h}\|$ and
¹⁶⁵ $\hat{\rho}^c(\mathbf{h})$ versus $\|\mathbf{h}\|$ are plotted in Figure 4; the true coefficient is drawn with a continuous line.
¹⁶⁶ In addition, for each value of $\|\mathbf{h}\|$, we included 90% confidence intervals based on quantiles
¹⁶⁷ 5 and 95 of the simulation values. The estimates of the SCCC were reasonably well-behaved
¹⁶⁸ but worsened when $\|\mathbf{h}\|$ was close to zero, as is typical of lag-dependent spatial functions
¹⁶⁹ computed over a rectangular grid where the minimum distance between coordinates is fixed.
¹⁷⁰ We also ran Monte Carlo simulations using the bivariate Matérn covariance function; the results
¹⁷¹ were similar. The estimate of ρ_{XY} was better for the Matérn case in terms of the mean square
¹⁷² error. With either covariance function, however, the estimates of ρ_{XY} affected the estimates of
¹⁷³ the SCCC.

¹⁷⁴ For the same region used in the previous Monte Carlo simulation, we computed the asymptotic
¹⁷⁵ variance of $\hat{\rho}^c(\cdot)$. For $0 < \|\mathbf{h}\| < 2$, all variances were less than 0.006, and the largest
¹⁷⁶ discrepancies between cases 1–4 were seen near the origin.

Table 1: Theoretical values, parameter estimates and standard errors (in parentheses) for the four cases considered in the simulation study in which we generated realizations of a random Gaussian random field with a bivariate Wendland-Gneiting covariance function

Case 1	$\sigma_1^2 = 1$	$\sigma_2^2 = 1$	$\rho_{12} = -0.15$	$b_1 = 0.5$	$b_{12} = 0.35$	$b_2 = 0.4$
	0.9906 (0.0896)	0.9995 (0.0715)	-0.1493 (0.0507)	0.4994 (0.0369)	0.3707 (0.1772)	0.4511 (0.1451)
Case 2	$\sigma_1^2 = 1$	$\sigma_2^2 = 1$	$\rho_{12} = 0.25$	$b_1 = 1.2$	$b_{12} = 0.9$	$b_2 = 1$
	1.0039 (0.2034)	1.0011 (0.1706)	0.2439 (0.1274)	1.2137 (0.1876)	1.0711 (0.3884)	0.9528 (0.3172)
Case 3	$\sigma_1^2 = 1$	$\sigma_2^2 = 1$	$\rho_{12} = 0.3$	$b_1 = 1.8$	$b_{12} = 1.4$	$b_2 = 1.5$
	0.9901 (0.1744)	1.0003 (0.00922)	0.3092 (0.3892)	1.7973 (0.5574)	1.4829 (0.2836)	1.4811 (0.2483)
Case 4	$\sigma_1^2 = 2$	$\sigma_2^2 = 0.5$	$\rho_{12} = 0.45$	$b_1 = 1.1$	$b_{12} = 0.9$	$b_2 = 1$
	1.9998 (0.3810)	0.4960 (0.0798)	0.4379 (0.0955)	1.1073 (0.1641)	0.9347 (0.4215)	1.1606 (0.3298)

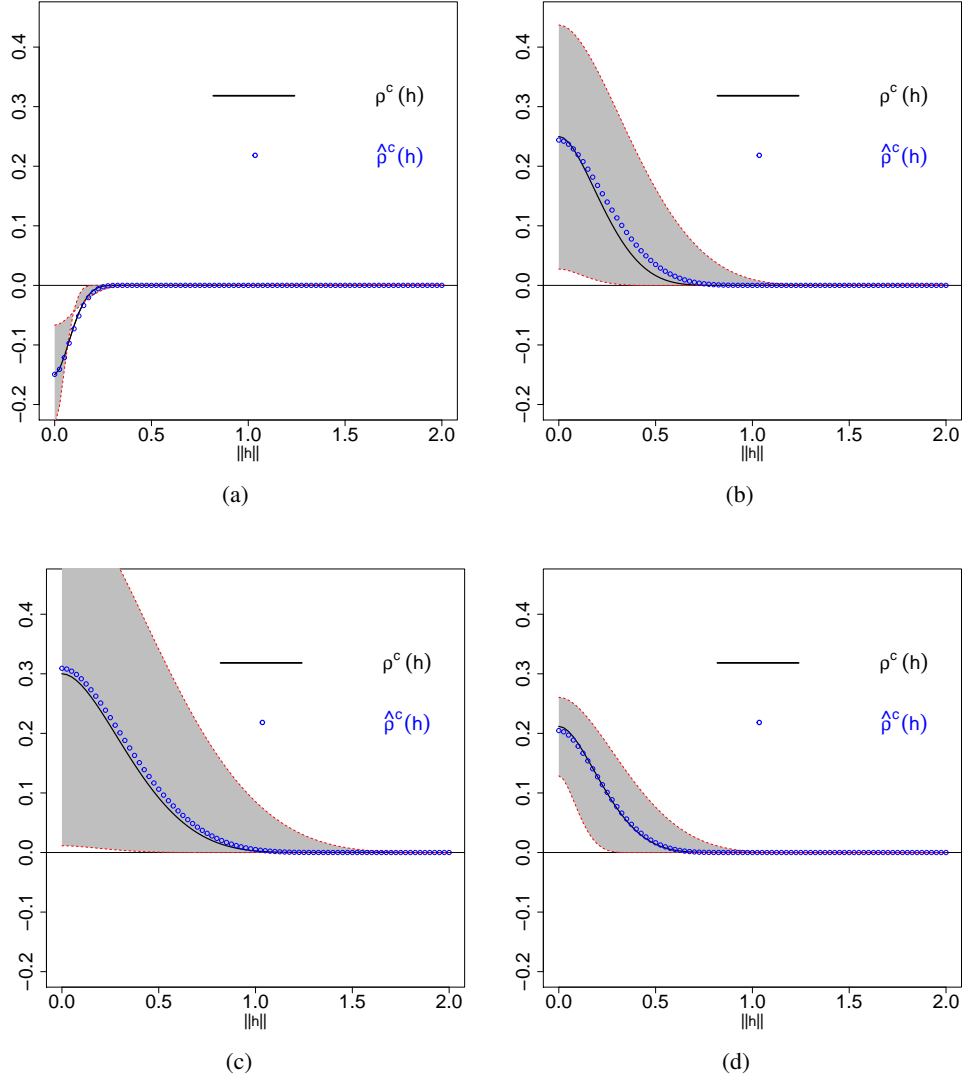


Figure 4: Theoretical coefficients (solid lines) and estimates (circles) for the distinct sets of parameters, with a 90% confidence interval based on quantiles 5 and 95. (a) Case 1; (b) Case 2; (c) Case 3; (d) Case 4.

177 For the local approach, we generated 100 replicates from a bivariate Gaussian random field
 178 sampled on a regular lattice of size 100×100 in the region $[0, 100]^2$, with mean equal to zero
 179 and Wendland-Gneiting covariance given in equation (9). We then split each process into 25
 180 square sub-images of size 10×10 , and estimated the parameters of the covariance function
 181 for each sub-image using ML. We also computed the local SCCC given by equations (14)
 182 and (15). Figure 5 illustrates box-plots of the estimates of σ_X , σ_Y , ρ_{XY} and b_{XY} for the 25
 183 sub-images for case 3, where the true parameters were $v = 4$, $k = 1$, $\sigma_X = \sigma_Y = 1$, $\rho_{XY} = 0.3$,
 184 $b_X = 1.8$, $b_Y = 1.4$, and $b_{XY} = 1.5$. Although the estimates did vary, the average values of all

185 sub-images were reasonably close to the true values. Finally, we computed $\hat{\rho}_1(\mathbf{h})$ and $\hat{\rho}_2(\mathbf{h})$
186 given by equations (14) and (15), and compared them with the global SCCC (Figure 6)

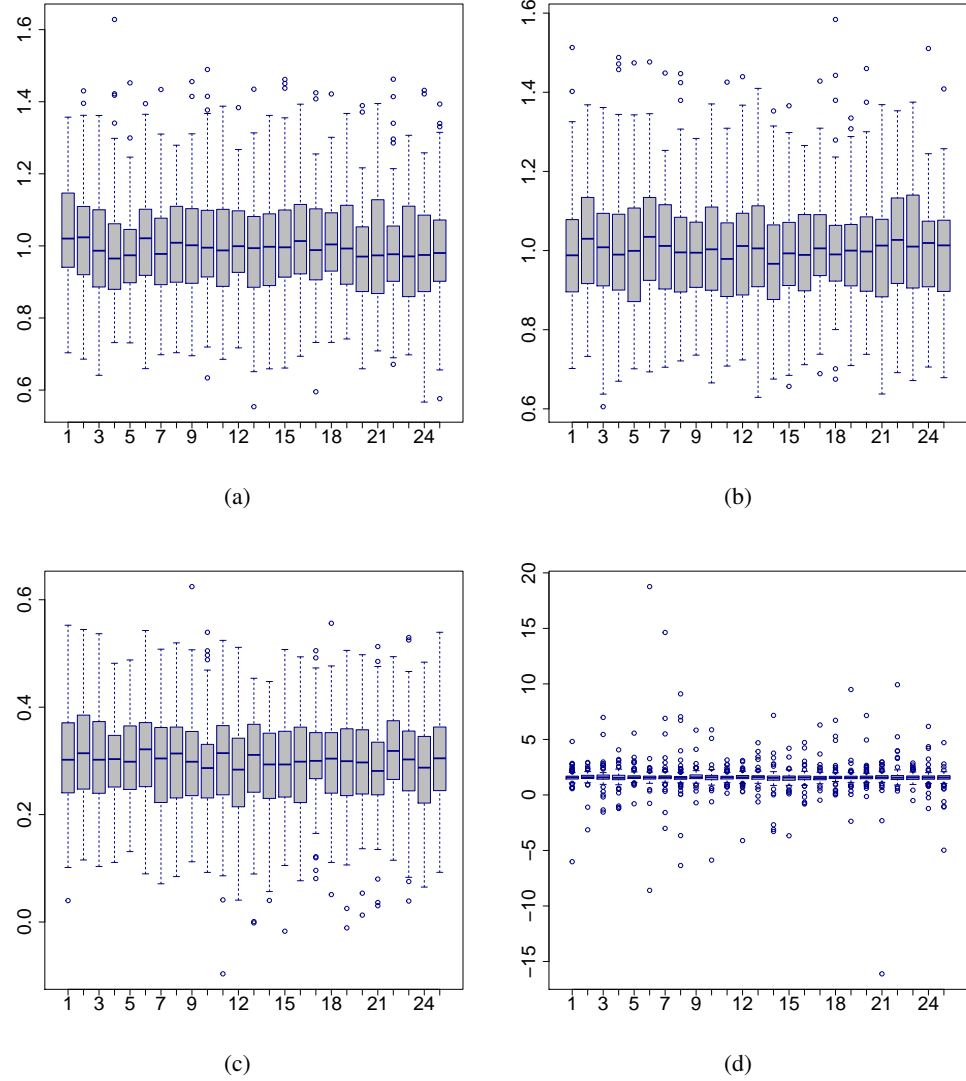


Figure 5: Box-plot for the estimates of the covariance parameters in each of the 25 sub-images. (a) σ_X ; (b) σ_Y ; (c) ρ_{XY} and (d) b_{XY} .

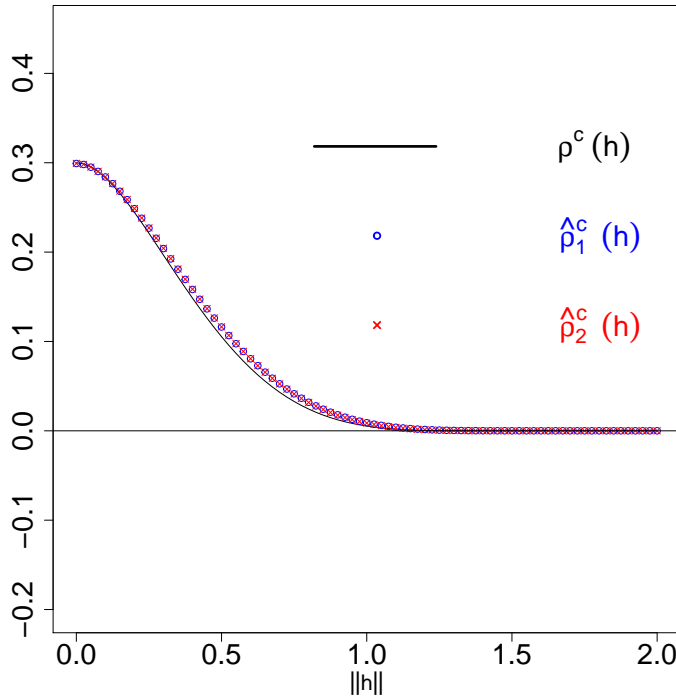


Figure 6: Local SCCC estimates (red and blue lines) and global theoretical SCCC (black) for a Gaussian spatial process with Wendland-Gneiting covariance function.

187 To observe the performance of the estimates of SCCC for an increasing domain framework,
 188 we did another Monte Carlo simulation study. Five hundred simulation runs from a zero-mean
 189 Gaussian random field with a Wendland-Gneiting covariance function with parameters $\nu = 4$,
 190 $k = 1$, $\sigma_X = \sigma_Y = 1$, $\rho_{XY} = 0.3$, $b_X = 1.8$, $b_Y = 1.4$, and $b_{XY} = 1.5$, were generated. We
 191 ran the simulations for the following six regions: $[1,4]^2$, $[1,8]^2$, $[1,12]^2$, $[1,16]^2$, $[1,20]^2$ and
 192 $[1,24]^2$, with 16, 64, 144, 256, 400 and 576 points respectively. Then in each simulation
 193 run, the ML estimations of the parameters of the SCCC were computed together with 90%
 194 confidence intervals based on the 5th and 95th quantiles. Estimates improve as the domain
 195 increases, yielding thinner confidence intervals (Figure 7).

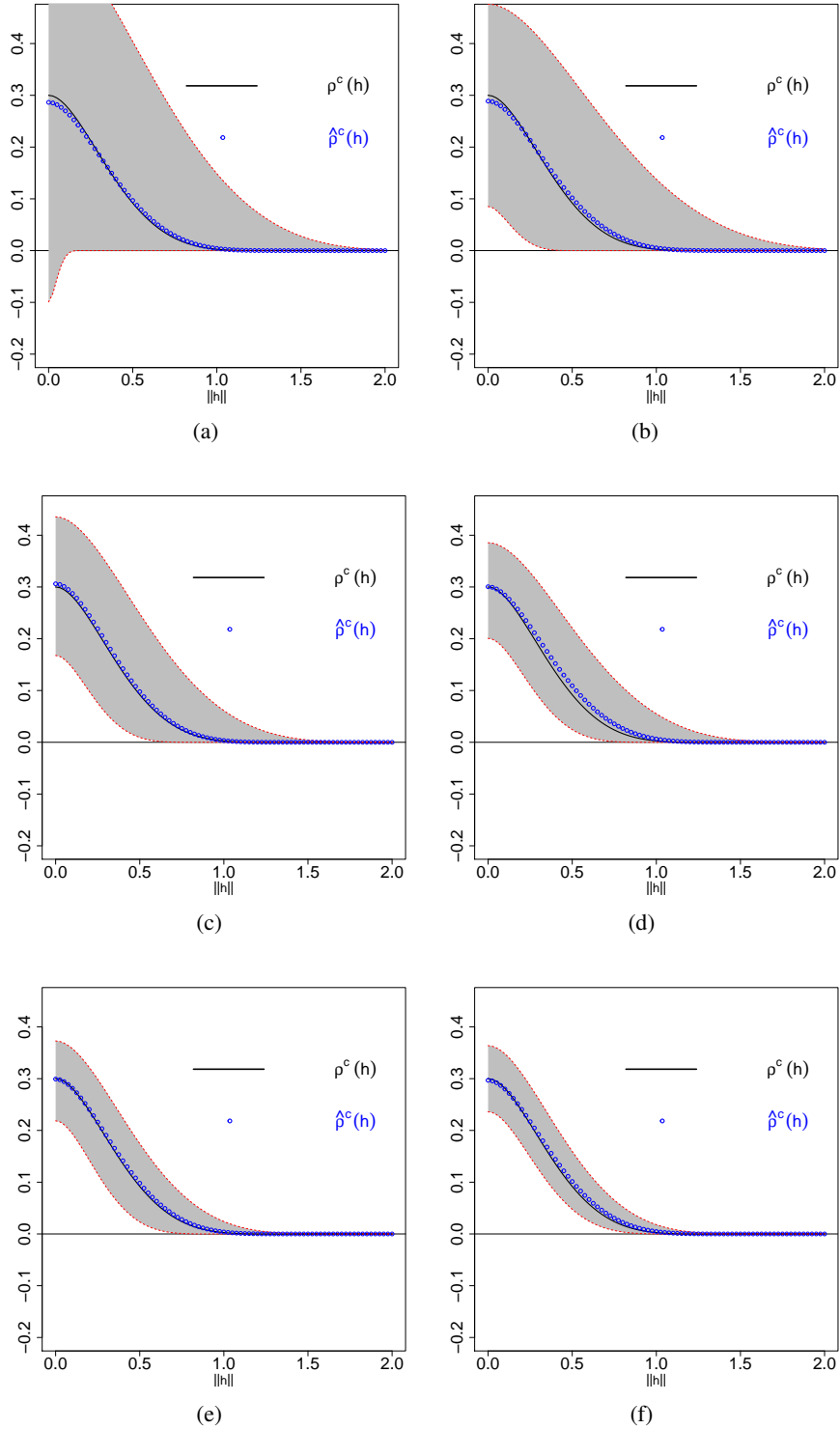


Figure 7: Theoretical SCCC (black line) and estimates (blue circles) for the distinct regions, with a confidence interval of 90 %. (a) 4x4 grid ; (b) 8x8 grid; (c) 12x12 grid; (d) 16x16 grid; (e) 20x20 grid ; (f) 24x24 grid.

196 To gain insight into the computational time required for computing $\hat{\rho}^c(\cdot)$ for the covariance
 197 functions used in this work, we ran similar simulations with different window sizes. We ran
 198 100 simulations for window sizes = 8×8 , 12×12 , 16×16 , and 20×20 . In each, $\hat{\rho}^c(\cdot)$ was
 199 computed for the Matérn and Wendland-Gneiting covariance functions. All computations were
 200 done using an HP ProLiant DL380G9 server, equipped with a 2x Intel Xeon E5-2630 v3 2.40
 201 GHz processor, 128 GB DDR4 2.133 Ghz RAM, and 512 GB SSD storage.

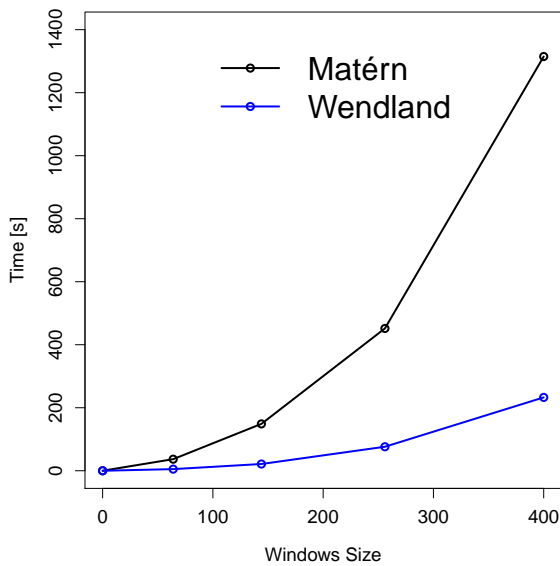


Figure 8: Computational time in seconds to compute $\hat{\rho}^c(\cdot)$ for the Matérn and Wendland-Gneiting covariance functions.

202 Time to run each simulation increased exponentially with window size (Figure 8). Al-
 203 though the time required to compute the Wendland-Gneiting covariance function was always
 204 smaller than the time to compute the Matérn covariance function, for real images it is not feasi-
 205 ble to compute $\hat{\rho}^c(\cdot)$, at least using an interpreted language such as R, which we used here. It is
 206 expected to find this kind of drawback for the Matérn covariance function because of the com-
 207 plexity of the model, the number of parameters, and the large amount of data. The compact
 208 support covariance functions (as in the Wendland model) reduces the computational burden
 209 ([Wendland, 1995](#)).

210 This result further supports the use of the local approach we presented in Section 5, but we
 211 plan to explore ways to optimize and accelerate the computation of $\hat{\rho}^c(\cdot)$.

212 7. An Application

213 7.1. Motivation

214 Our application derives from ecology. In order to track the seasonality (“phenology”)
 215 of vegetation in different ecosystems, digital cameras have been deployed to record high-
 216 frequency images of the canopy at hundreds of research sites around the world ([Richardson,](#)

217 2018). From each image, color-channel information (e.g., RGB [red-green-blue] values of each
218 pixel) are extracted and converted to a suite of “vegetation indices” derived from linear or non-
219 linear transformations of the RGB or other color spaces (Sonnenstag et al., 2012; Mizunuma
220 et al., 2014; Toomey et al., 2015; Nguy-Robertson et al., 2016). These indices have been used
221 to identify the timing of seasonal phenomena such as leaf-out, senescence, and abscission,
222 and to monitor how these phenomena are changing in response to ongoing climatic change
223 (Sonnenstag et al., 2012). However, different cameras may render the same scene differently
224 because of the specifics of the imaging sensor being used (e.g., CCD, CMOS) and researchers
225 have used a wide range of different cameras because of considerations including trade-offs be-
226 tween cost and image quality. Changes in scene illumination (e.g., caused by time-of-day or
227 cloud cover) also may impact the resulting image. Although previous research has shown that
228 diurnal, seasonal, and weather-related changes in illumination can have large effects on esti-
229 mates of average color (or color index) for the whole image or a region of interest (Sonnenstag
230 et al., 2012), spatial information has not been incorporated previously in these estimates.

231 *7.2. Imagery*

232 We focus here on comparing two jpeg images taken of the same scene on 20 October 2010
233 by two different cameras (Figures 9(a), 9(b)). These images were taken with, respectively, an
234 outdoor StarDot NetCam XL 3MP camera with a 2048×1636 -pixel CMOS sensor (Figure
235 9(a)) and an outdoor Axis 223M camera with a 1600×1200 -pixel CCD sensor (Figure 9(b)).
236 These images were selected from the image archive associated with an experiment, analyzed
237 and reported on previously by Sonnenstag et al. (2012), in which images, color time series, and
238 phenological transition dates from eleven different cameras were compared. Although the two
239 images we use here are of the same scene and were taken at the same time, they are not iden-
240 tical. For example, both cameras were pointing due north with an $\approx 20^\circ$ tilt angle, but image
241 displacement occurred because the cameras were mounted at different positions on a fixed plat-
242 form. The resolution and overall field-of-view also differed because of different sensor sizes
243 and lens characteristics. Sonnenstag et al. (2012) compared color information averaged across a
244 small “region of interest” in the images. Here, we work with the entire images after correction
245 for differences of field-of-view and displacement.



(a)

(b)

Figure 9: Two images taken by adjacent cameras of the same site at Harvard Forest. (a): Image taken with an outdoor StarDot NetCam XL 3MP camera. (b): Image taken with an outdoor Axis 223M camera. The dominant tree species (foreground) is red oak (*Quercus rubra*), and there is some white pine (*Pinus strobus*) in the upper right corner.

246 To account for differences in field-of-view and displacement, the two images were first
 247 manually cropped using tools in IrfanView (version 4.38; [Skiljan 2014](#)) to equivalent areas and
 248 aspect ratios. The resulting images had 2023×1444 pixels for the higher-resolution one taken
 249 with the StarDot camera and 1297×922 pixels for the lower-resolution one taken with the
 250 Axis camera. The higher-resolution image was then resized and down-sampled in IrfanView
 251 so that it had the same number of pixels as the lower-resolution image (Figures 10(a), 10(b)).
 252 These two images were loaded into the R software system (version 3.51; [R Core Team, 2018](#))
 253 using the `load.image` function in the `imager` package ([Urbanek, 2014](#)) and transformed either
 254 to gray-scale using the `grayscale` function in the same package (Figures 11(a), 11(b)) or to
 255 green chromatic coordinates ($g_{cc} = \frac{G}{R+G+B}$), which normalizes for brightness ([Gillespie et al.,
 256 1987](#)) (Figures 12(a), 12(b)). For both the gray-scale and g_{cc} images, the lower-resolution
 257 image (Figures 11(b) and 12(b), respectively) was then coordinate-registered to the higher-
 258 resolution image (Figure 11(a) and 12(a), respectively) using the R package `RNiftyReg` and
 259 a linear (affine) transformation with 12 degrees of freedom ([Clayton et al., 2018](#)). Spatial
 260 concordance was assessed between the resampled higher-resolution images (Figure 11(a) or
 261 12(a)) and the coordinate-registered lower-resolution images (Figure 11(c) or 12(c)).



Figure 10: The two images from Harvard Forest after cropping to equivalent views and resampling to equivalent pixel dimensions. (a): Image taken with an outdoor StarDot NetCam XL 3MP camera (Figure 9(a)); (b): Image taken with an outdoor Axis 223M camera (9(b)).

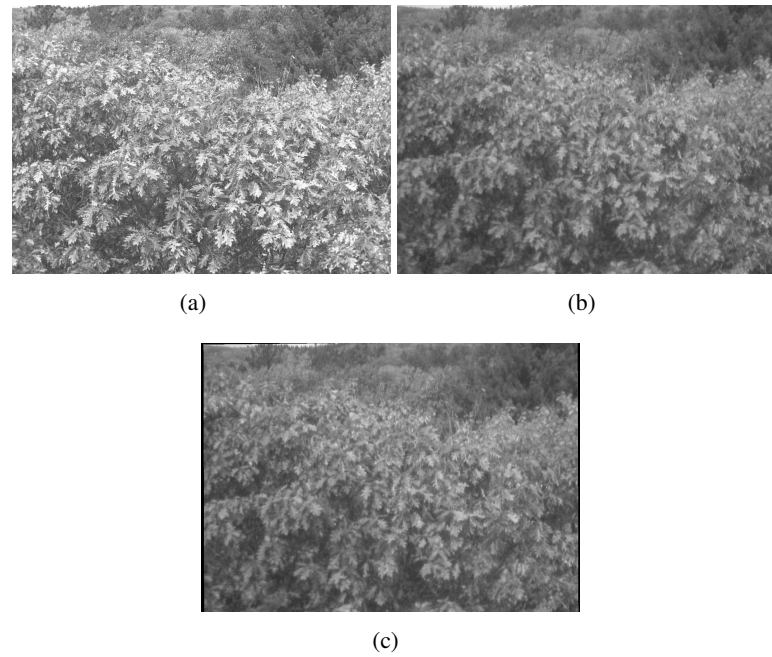


Figure 11: The two cropped and resampled images (Figures 10(a), 10(b)) converted to grayscale, and the coordinate registration of the second image with respect to the first. (a): Image taken with an outdoor StarDot NetCam XL 3MP camera (Figure 10(a)); (b): Image taken with an outdoor Axis 223M camera (Figure 10(b)); (c): Image (b) registered to image (a).

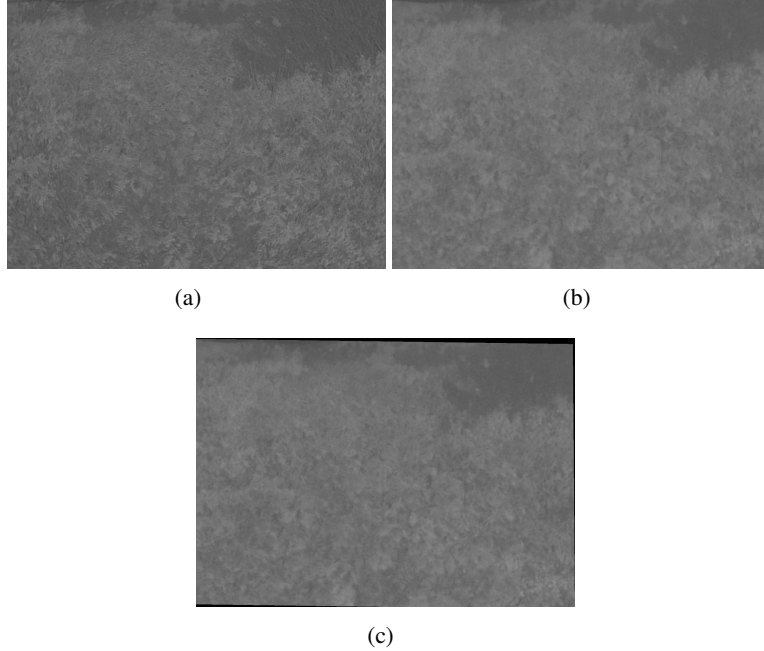


Figure 12: Cropped and resampled images (Figures 10(a), 10(b)) corrected for brightness using the green chromatic coordinate (g_{cc}), and the coordinate registration of the second image with respect to the first. (a): g_{cc} for Figure 10(a); (b): g_{cc} for Figure 10(b); (c): Image (b) registered to image (a).

262 7.3. Estimating concordance

263 For each pair of images, we first calculated Lin’s (1989) CCC. We then calculated the
 264 SCCC as described in Section 5. We calculated the local concordance coefficient $\rho_i(\cdot)$ in
 265 small (12×12 -pixel) non-overlapping windows. To fit the local model to each small window,
 266 we used a Gaussian process $Z(s) = (X(s), Y(s))^\top$, $s \in \mathbb{R}^2$, with mean $(\mu_X, \mu_Y)^\top$ and the
 267 covariance functions described in equations (6)–(9). We used the function `GeoFit` in the R
 268 package `GeoModels` (Bevilacqua and Morales-Oñate, 2018) to compute the ML estimators of
 269 the parameters involved in the models. For computational efficiency, the Matérn and Wendland-
 270 Gneiting covariances were estimated for a randomly-selected set of 1,467 20×20 -pixel sub-
 271 images; the model to be used was selected based on the Akaike and Bayesian Information
 272 Criteria (AIC and BIC, respectively). In general, the AIC and BIC coefficients were smaller for
 273 estimates using the Matérn covariance than for the Wendland-Gneiting covariance, and so we
 274 used the Matérn model even though it took somewhat more time to use it to compute the local
 275 estimators. Finally, the global SCCCs for each pair of images were estimated using equations
 276 (14) and (15).

277 7.4. Estimates of concordance

278 Lin’s coefficient was $\rho_c = 0.1334$ for the grayscale images (Figures 11(a) vs. 11(c)) and
 279 $\rho_c = 0.2450$ for the g_{cc} -indexed images (Figures 12(a) vs. 12(c)). In Figure 13 we plot Lin’s
 280 coefficient and the two global coefficients as a function of the spatial norm. We observed a

281 rapid decay of $\hat{\rho}_2(\cdot)$ and a slower decay of $\hat{\rho}_1(\cdot)$. The decay was related to the way in which
 282 the estimates were computed for each window: $\hat{\rho}_1(\cdot)$ is a coefficient obtained by plugging
 283 in the average of the parameters in the concordance function, but $\hat{\rho}_2(\cdot)$ is the average of the
 284 concordance using all possible windows.

285 For $\|h\| = 0$, we observed that the SCCC was approximately one-third ($0.08/0.245 \times 100 \approx 0.33$) of Lin's CCC. This suggests that Lin's CCC overestimated the spatial concordance
 286 between these two images, and implies that it would be inappropriate to use it for modeling
 287 spatial data.

288 It is also worth mentioning that the low SCCC between two images like these—high-resolution
 289 *versus* low-resolution registered to high-resolution—implies that even at small lags there is substantial information lost in the post-processing of the lower-resolution image. Thus,
 290 one should be cautious in trying to up-scale information from either lower-resolution imagery
 291 or similar (e.g., historical) datasets. We are unlikely to be able to extract more information
 292 from an image than is actually contained within it.

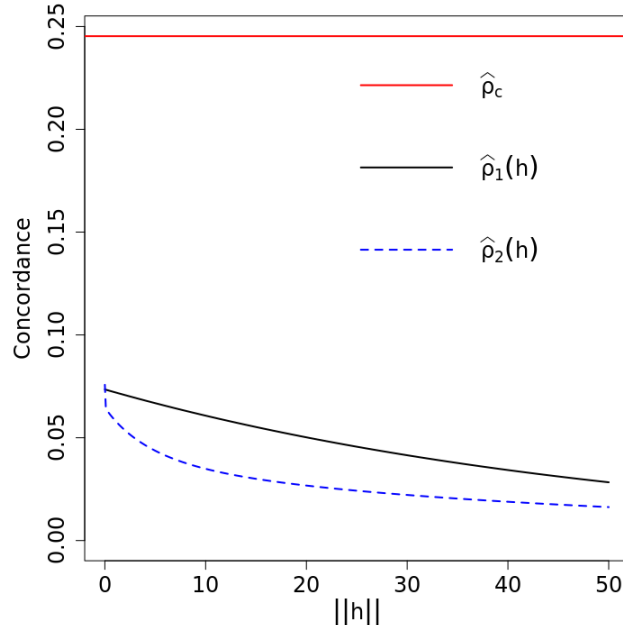


Figure 13: Global concordance coefficients and Lin's CCC for the g_{cc} -indexed images.

295 We also note that the development of hypothesis testing about the SCCC using Theorem
 296 1 requires the computation of the asymptotic variance, which could be complicated for an
 297 arbitrary v . Resampling methods provide alternatives that could help estimate the asymptotic
 298 variance of the sample version of the SCCC. Castillo-Páez et al. (2019) presents recent work
 299 along these lines in a spatial framework.

300 The images and all the code used in this paper are available from the Environmental Data
 301 Initiative doi:[10.6073/pasta/4a975798efc9e099104a1e4391f73574](https://doi.org/10.6073/pasta/4a975798efc9e099104a1e4391f73574).

302 **8. Discussion**

303 With the work presented herein, we have extended the standard methodology for estimating
304 concordance into the spatial domain. Our approach consisted in defining a new coefficient that
305 preserves the interpretation of Lin's (1989) concordance correlation coefficient (CCC) for two
306 spatial variables and for a fixed spatial lag. Our new spatial concordance correlation coefficient
307 (SCCC) compares the correlation between two spatial variables with respect to their fit to a
308 45° line that passes through the origin. The properties of Lin's (1989) CCC are inherited by
309 our SCCC. The ML estimator of our SCCC for the Wendland-Gneiting covariance function is
310 asymptotically normal for an increasing domain sampling scheme. We defined a local SCCC
311 and established its asymptotic normality for the sample version. From the local SCCC, we de-
312 rived two estimates for the overall SCCC, one based on the average of the p local coefficients
313 and the other based on the average of the parameters in the correlation function. Deriving the
314 global SCCC from local coefficients estimated in small non-overlapping windows is computa-
315 tionally more efficient and permits the estimation of spatial concordance for large images that
316 are used commonly in a wide range of applications.

317 The Monte Carlo simulation study presented in Section 6 revealed that for the Matérn and
318 Wendlang-Gneiting covariance functions, the sample version of the SCCC produced accurate
319 estimates of the SCCC that decreased with distance (spatial lag). However, the time required
320 to compute SCCC grows exponentially with window size, implying that for a large image size
321 it is unfeasible to compute $\hat{\rho}(\cdot)$ using an interpreted language like R. Although we are explor-
322 ing ways to improve computational efficiency, the local approach introduced here (Section 5)
323 appears to be a straightforward way to estimate SCCC for large images.

324 The camera comparison experiment conducted by Sonnentag et al. (2012) found that im-
325 ages recorded with a variety of different camera makes and models, all mounted on the top of
326 the same canopy access tower and with a similar field of view, varied in visual appearance, in-
327 cluding color balance, saturation, contrast, and brightness. These differences can be attributed
328 to internal differences in sensor design and image processing, and external factors such as light-
329 ing. However, Sonnentag et al. (2012) also found that when simple normalized indices were
330 calculated from the image data, and the emphasis was placed on the seasonality—rather than
331 absolute magnitude—of those indices, the phenological information derived from the imagery
332 was extremely similar across all cameras. Notably, their analysis focused on information about
333 the average color across a large “region of interest” drawn across the canopy (Sonnentag et al.,
334 2012). Although this approach is widely used (Richardson, 2018) and it has the advantage of
335 enabling integration across multiple individuals or species that may comprise a typical forest
336 canopy, it lacks spatial information.

337 The SCCC we developed and presented here summarizes and accounts for the spatial infor-
338 mation in the images, permitting more rigorous characterization of agreement between high-
339 resolution digital images recorded by different sensors. Other applications include using im-
340 ages from different satellite remote-sensing platforms as part of ongoing efforts to harmonize,
341 for example, imagery with different spatial resolution, spectral sensitivity, and angular char-
342 acteristics (e.g., Landsat-Sentinel efforts: Claverie et al., 2018). Calculation of concordance
343 statistics before and after sensor harmonization could provide critical and objective informa-
344 tion about the success of different harmonization methods. There also could be potential appli-

345 cations in the fusion of remotely-sensed data obtained at different spatiotemporal resolutions,
 346 such as MODIS with its 500-m spatial resolution and daily temporal resolution, and Landsat
 347 with its 30-m spatial resolution and 16-day temporal resolution (Gao et al., 2015). Another
 348 application in ecology in which the SCCC coefficient could be used is for improving census
 349 information or better estimating detection probability of mobile organisms captured on camera
 350 traps. The aim could be to try to match animal coat or skin markings to reliably identify a
 351 re-sighting of the same individual *versus* different ones. In environmental sciences it is also
 352 of interest to test the agreement between different sensors that measure air quality in polluted
 353 cities. For example, Santiago, Chile has only 12 air-quality monitoring stations (The World Air
 354 Quality Index project: <http://aqicn.org/contact/es/>). The need for new stations makes
 355 relevant the spatial concordance analysis between different types of sensors in a calibration
 356 context.

357 An important part of the analysis of agreement between two images using the SCCC is the
 358 pre-processing applied to the images before computing the concordance index. Most filters
 359 deteriorate the spatial information contained in both images. Concordance indices calculated
 360 after image processing capture only relationships between the remaining patterns and could
 361 yield low concordance values that underestimate the real spatial agreement. The question of
 362 what kind of filters preserve spatial concordance is left as an open problem to be tackled in
 363 future research as, to the best of our knowledge, this problem has not yet been treated in the
 364 image-processing literature.

Another important aspect in modeling the spatial concordance between images is their subdivision into small windows to estimate the SCCC using a local approach. We are aware that when fitting each window using a different Matérn model, there is no continuity of the smoothing parameters. Therefore, two contiguous processes could have very different estimates of the smoothing parameters, producing a discontinuity at their edges. One way to approach this problem is to use the local likelihood to define a smoothing function in the lines (Anderes and Stein, 2011). With respect to the estimation of the bivariate Matérn model, we observed that when all parameters were estimated, the ML estimates could be highly inefficient. Thus, we agree with Gneiting et al. (2010) that the best predictive models tend to be the most parsimonious, subject to retention of key characteristics, such as the negative dependency between the two process components (see also Makridakis and Taleb, 2009). Finally, the selection of the spatial lag \mathbf{h} is crucial if there is no information about which direction to prefer. One way to approach this issue is to consider an average of spatial concordance values corresponding to the four cardinal directions with respect to the origin (Vallejos et al., 2015), i.e., for $\mathbf{h}_1 = (1, 0)$ and $\mathbf{h}_2 = (0, 1)$, we can define the average concordance coefficient as

$$\rho_{AV}^c(\mathbf{h}_1, \mathbf{h}_2) := \frac{1}{4} [\rho^c(\mathbf{h}_1) + \rho^c(-\mathbf{h}_1) + \rho^c(\mathbf{h}_2) + \rho^c(-\mathbf{h}_2)].$$

365 9. Future Work

366 Several related theoretical and applied problems arise from the methodology suggested in
 367 this article that would be fruitful directions for future research. First, SCCC could be applied to
 368 images taken at two points in time by the same camera. The decay of the SCCC as a function
 369 of the norm would be expected to be similar to that seen in Figure 13 for each sequential

pair of images. Another approach for dealing with the same problem would be to consider a sequence of n images taken with the same camera to be a spatiotemporal process. Then, the SCCC and its estimation properties could be studied in that context. This generalization of the SCCC would have applications in, for example, spatiotemporal analysis of satellite images taken weeks, months, or years apart as a way of characterizing patterns of landscape change.

Acknowledgments

This work has been partially supported by the AC3E, UTFSM, under grant FB-0008, and by grants to A.D.R. from the US National Science Foundation (EF-1065029, EF-1702697, DEB-1237491) and the United States Geological Survey (G10AP00129). This is a contribution from the Harvard Forest Long-term Ecological Research (LTER) site, supported most recently by the US National Science Foundation (DEB 18-32210).

Appendix

Mardia and Marshall Theorem

Let $\{Y(\mathbf{s}) : \mathbf{s} \in D \subset \mathbb{R}^d\}$ be a Gaussian random field such that $Y(\cdot)$ is observed on $D_n \subset D$. It is assumed that D_n is a non-random set satisfying $\|\mathbf{s} - \mathbf{t}\| \geq \gamma > 0$ for all $\mathbf{s}, \mathbf{t} \in D_n$. This ensures that the sampling set is increasing as n increases. Denote $\mathbf{Y} = (Y(\mathbf{s}_1), \dots, Y(\mathbf{s}_n))^\top$ and assume that $\mathbb{E}[\mathbf{Y}] = \mathbf{X}\boldsymbol{\beta}$, $\text{cov}(Y(\mathbf{t}), Y(\mathbf{s})) = \sigma(\mathbf{t}, \mathbf{s}; \boldsymbol{\theta})$, \mathbf{X} is $n \times p$ with $\text{rank}(\mathbf{X}) = p$, $\boldsymbol{\beta} \in \mathbb{R}^p$, and $\boldsymbol{\theta} \in \Theta$, where Θ is an open set of \mathbb{R}^q . Let $\Sigma = \Sigma(\boldsymbol{\theta})$ be the covariance matrix of \mathbf{Y} such that the ij -th element of Σ is $\sigma_{ij} = \sigma(\mathbf{s}_i, \mathbf{s}_j; \boldsymbol{\theta})$. We can estimate $\boldsymbol{\theta}$ and $\boldsymbol{\beta}$ using ML, by maximizing

$$L = L(\boldsymbol{\beta}, \boldsymbol{\theta}) = k - \frac{1}{2} \ln |\Sigma| - \frac{1}{2} (\mathbf{Y} - \mathbf{X}\boldsymbol{\beta})^\top \Sigma^{-1} (\mathbf{Y} - \mathbf{X}\boldsymbol{\beta}), \quad (\text{A.1})$$

where k is a constant.

Let $\mathbf{L}_n^{(1)} = \nabla L = (\mathbf{L}_{\boldsymbol{\beta}}^\top, \mathbf{L}_{\boldsymbol{\theta}}^\top)^\top$ and

$$\mathbf{L}_n^{(2)} = \begin{pmatrix} \mathbf{L}_{\boldsymbol{\beta}\boldsymbol{\beta}} & \mathbf{L}_{\boldsymbol{\beta}\boldsymbol{\theta}} \\ \mathbf{L}_{\boldsymbol{\theta}\boldsymbol{\beta}} & \mathbf{L}_{\boldsymbol{\theta}\boldsymbol{\theta}} \end{pmatrix}$$

be the gradient vector and Hessian matrix, respectively, obtained from equation (A.1). Let $\mathbf{F}_n = -\mathbb{E}[\mathbf{L}_n^{(2)}]$ be the Fisher information matrix with respect to $\boldsymbol{\beta}$ and $\boldsymbol{\theta}$. Then, $\mathbf{F}_n = \text{diag}(\mathbf{F}_n(\boldsymbol{\beta}), \mathbf{F}_n(\boldsymbol{\theta}))$, where $\mathbf{F}_n(\boldsymbol{\beta}) = -\mathbb{E}[\mathbf{L}_{\boldsymbol{\beta}\boldsymbol{\beta}}]$ and $\mathbf{F}_n(\boldsymbol{\theta}) = -\mathbb{E}[\mathbf{L}_{\boldsymbol{\theta}\boldsymbol{\theta}}]$.

For a twice differentiable covariance function $\sigma(\cdot, \cdot; \boldsymbol{\theta})$ on Θ with continuous second derivatives, Mardia and Marshall (1984) provided sufficient conditions on Σ and \mathbf{X} such that the limiting distribution of $(\widehat{\boldsymbol{\beta}}_n^\top, \widehat{\boldsymbol{\theta}}_n^\top)^\top$ is normal, per the following:

Theorem. Let $\lambda_1 \leq \dots \leq \lambda_n$ be the eigenvalues of Σ , and let those of $\Sigma_i = \frac{\partial \Sigma}{\partial \theta_i}$ and $\Sigma_{ij} = \frac{\partial^2 \Sigma}{\partial \theta_i \partial \theta_j}$ be λ_k^i and λ_k^{ij} , $k = 1, \dots, n$, such that $|\lambda_1^i| \leq \dots \leq |\lambda_n^i|$ and $|\lambda_1^{ij}| \leq \dots \leq |\lambda_n^{ij}|$ for $i, j = 1, \dots, q$. Suppose that as $n \rightarrow \infty$

- 393 (i) $\lim \lambda_n = C < \infty$, $\lim |\lambda_n^i| = C_i < \infty$ and $\lim |\lambda_n^{ij}| = C_{ij} < \infty$ for all $i, j = 1, \dots, q$.
 394 (ii) $\|\Sigma_i\|^{-2} = O(n^{-\frac{1}{2}-\delta})$ for some $\delta > 0$, for $i = 1, \dots, q$.
 395 (iii) For all $i, j = 1, \dots, q$, $a_{ij} = \lim [t_{ij}/(t_{ii}t_{jj})^{\frac{1}{2}}]$ exists, where $t_{ij} = \text{tr}(\Sigma^{-1}\Sigma_i\Sigma^{-1}\Sigma_j)$ and
 396 $\mathbf{A} = (a_{ij})$ is nonsingular.
 397 (iv) $\lim(\mathbf{X}^\top \mathbf{X})^{-1} = \mathbf{0}$.

398 Then, $(\widehat{\boldsymbol{\beta}}_n^\top, \widehat{\boldsymbol{\theta}}_n^\top)^\top \xrightarrow{\mathcal{L}} \mathcal{N}((\boldsymbol{\beta}^\top, \boldsymbol{\theta}^\top)^\top, \mathbf{F}_n^{-1})$ as $n \rightarrow \infty$, in an increasing domain sense.

399 **Proof of Theorem 1**

400 The proof consists of verifying the [Mardia and Marshall \(1984\)](#) conditions. In Theorem
 401 1, $\mathbb{E}[\mathbf{Z}(s)] = \mathbf{0}$; thus the fourth condition in Mardia and Marshall's [1984](#) theorem (above),
 402 $\lim(\mathbf{X}^\top \mathbf{X})^{-1} = \mathbf{0}$, is trivially satisfied. Satisfying the first three conditions is somewhat more
 403 complex.

For the first two conditions, we start by considering v to be fixed. Then

$$\begin{aligned} C_X(\mathbf{h}) &= \sigma_X^2 \left(1 + (v+1) \frac{\|\mathbf{h}\|}{b_X} \right) \left(1 - \frac{\|\mathbf{h}\|}{b_X} \right)_+^{v+1}, \\ C_Y(\mathbf{h}) &= \sigma_Y^2 \left(1 + (v+1) \frac{\|\mathbf{h}\|}{b_Y} \right) \left(1 - \frac{\|\mathbf{h}\|}{b_Y} \right)_+^{v+1}, \\ C_{XY}(\mathbf{h}) &= C_{YX}(\mathbf{h}) = \rho_{XY} \sigma_X \sigma_Y \left(1 + (v+1) \frac{\|\mathbf{h}\|}{b_{XY}} \right) \left(1 - \frac{\|\mathbf{h}\|}{b_{XY}} \right)_+^{v+1}. \end{aligned}$$

404 Let us consider an increasing domain scenario for process $\mathbf{Z}(s)$, with points s_1, \dots, s_n located in a rectangle $D_n \subset \Delta \mathbb{Z}^d$, for $0 < \Delta < \infty$, and $D_n \subset D_{n+1}$, for all n .
 405

Define the distance matrix $\mathbf{H}_n = [H_{lq}]_{l,q=1}^n$, where $H_{lq} = \|s_l - s_q\|$, and $\|\cdot\|$ denotes the Euclidean norm. Then the covariance matrix of $(\mathbf{Z}(s_1)^\top, \dots, \mathbf{Z}(s_n)^\top)^\top$ can be written as

$$\Sigma_n(\boldsymbol{\theta}) = \begin{pmatrix} \sigma_X^2 & \sigma_X \sigma_Y \rho_{XY} \\ - & \sigma_Y^2 \end{pmatrix} \otimes \boldsymbol{\Gamma}_n,$$

where $\boldsymbol{\Gamma}_n = \left[\left(1 + \frac{(v+1)H_{lq}}{b_{XY}} \right) \left(1 - \frac{H_{lq}}{b_{XY}} \right)_+^{v+1} \right]_{l,q=1}^n$ and $\boldsymbol{\theta} = (\sigma_X^2, \sigma_Y^2, \rho_{XY}, b_{XY})^\top$. Taking derivatives, we obtain

$$\begin{aligned} \frac{\partial \Sigma_n(\boldsymbol{\theta})}{\partial \sigma_X^2} &= \begin{pmatrix} 1 & \frac{\sigma_Y \rho_{XY}}{2\sigma_X} \\ - & 0 \end{pmatrix} \otimes \boldsymbol{\Gamma}_n, & \frac{\partial \Sigma_n(\boldsymbol{\theta})}{\partial \sigma_Y^2} &= \begin{pmatrix} 0 & \frac{\sigma_X \rho_{XY}}{2\sigma_Y} \\ - & 1 \end{pmatrix} \otimes \boldsymbol{\Gamma}_n, \\ \frac{\partial \Sigma_n(\boldsymbol{\theta})}{\partial b_{XY}} &= \begin{pmatrix} \sigma_X^2 & \sigma_X \sigma_Y \rho_{XY} \\ - & \sigma_Y^2 \end{pmatrix} \otimes \mathbf{S}_n, & \frac{\partial \Sigma_n(\boldsymbol{\theta})}{\partial \rho_{XY}} &= \begin{pmatrix} 0 & \sigma_X \sigma_Y \\ - & 0 \end{pmatrix} \otimes \boldsymbol{\Gamma}_n, \end{aligned}$$

where S_n is given by

$$S_n = \frac{\partial \Gamma_n}{\partial b_{XY}} = \left[\frac{(\nu+1)H_{lq}}{b_{XY}^2} \left(1 - \frac{H_{lq}}{b_{XY}} \right)_+^\nu \left(- \left(1 - \frac{H_{lq}}{b_{XY}} \right)_+ + \left(1 + \frac{(\nu+1)H_{lq}}{b_{XY}} \right) \right) \right]_{l=q=1}^n.$$

For any matrix norm, the spectral radius $\lambda_{\max}\{\mathbf{A}\}$ of an $n \times n$ matrix \mathbf{A} satisfies $\lambda_{\max}\{\mathbf{A}\} \leq \|\mathbf{A}\|$. Then, considering the norm $\|\cdot\|_\infty$, we have

$$\begin{aligned} \lambda_{\max}\{\Gamma_n\} &\leq \|\Gamma_n\|_\infty = \max_l \sum_{q=1}^n \left| \left(1 + \frac{(\nu+1)H_{lq}}{b_{XY}} \right) \left(1 - \frac{H_{lq}}{b_{XY}} \right)_+^{\nu+1} \right| \\ &= \sup_{1 \leq l \leq n} \sum_{q=1}^n \left| \left(1 + \frac{(\nu+1)H_{lq}}{b_{XY}} \right) \left(1 - \frac{H_{lq}}{b_{XY}} \right)_+^{\nu+1} \right| \\ &< \sum_{s \in \Delta \mathbb{Z}^d} \left(1 + \frac{(\nu+1)\|s\|}{b_{XY}} \right) \left(1 - \frac{\|s\|}{b_{XY}} \right)_+^{\nu+1}. \end{aligned}$$

One can check that

$$\int_{s \in \mathbb{R}^d} \left(1 + \frac{(\nu+1)\|s\|}{b_{XY}} \right) \left(1 - \frac{\|s\|}{b_{XY}} \right)_+^{\nu+1} ds < \infty.$$

Thus $\sup_n \lambda_{\max}\{\Gamma_n\} < \infty$, which implies that $\sup_n \lambda_{\max}\{\Sigma_n(\boldsymbol{\theta})\} < \infty$. Because Γ_n is positive definite, $\lambda_i\{\Gamma_n\} > 0$, $i = 1, \dots, n$. In particular, $\lambda_{\min}\{\Gamma_n\} > 0$, so $\inf_n \lambda_{\min}\{\Gamma_n\} > 0$ and $\inf_n \lambda_{\min}\{\Sigma_n\} > 0$. Further,

$$\sup_n \lambda_{\max} \left\{ \frac{\partial \Sigma_n(\boldsymbol{\theta})}{\partial \sigma_X^2} \right\} = \sup_n \lambda_{\max} \left[\begin{pmatrix} 1 & \frac{\sigma_Y \rho_{XY}}{2\sigma_X} \\ - & 0 \end{pmatrix} \otimes \Gamma_n \right] < \infty, \text{ for } \frac{\sigma_Y \rho_{XY}}{2\sigma_X} < \infty.$$

Similarly,

$$\sup_n \lambda_{\max} \left\{ \frac{\partial \Sigma_n(\boldsymbol{\theta})}{\partial \sigma_Y^2} \right\}, \sup_n \lambda_{\max} \left\{ \frac{\partial \Sigma_n(\boldsymbol{\theta})}{\partial \rho_{XY}} \right\} < \infty.$$

Moreover, $\lambda_{\max}\{S_n\} \leq \|S_n\|_\infty < \infty$ because of the form of the polynomial in $s \in \mathbb{R}^d$ and the compact support in b_{XY} . Then, for $\sigma_X^2, \sigma_Y^2, \sigma_X \sigma_Y \rho_{XY} < \infty$,

$$\sup_n \lambda_{\max} \left\{ \frac{\partial \Sigma_n(\boldsymbol{\theta})}{\partial b_{XY}} \right\} < \infty.$$

This implies that,

$$\sup_n \lambda_{\max} \left\{ \frac{\partial \Sigma_n(\boldsymbol{\theta})}{\partial \theta_c} \right\} < \infty, \quad c = 1, 2, 3, 4.$$

The second derivatives are:

$$\begin{aligned}
\frac{\partial^2 \Sigma_n(\theta)}{\partial \sigma_X^2 \partial \sigma_Y^2} &= \begin{pmatrix} 0 & \frac{\rho_{XY}}{4\sigma_X \sigma_Y} \\ - & 0 \end{pmatrix} \otimes \Gamma_n, & \frac{\partial \Sigma_n(\theta)}{\partial \sigma_X^2 \partial b_{XY}} &= \begin{pmatrix} 1 & \frac{\sigma_Y \rho_{XY}}{2\sigma_X} \\ - & 0 \end{pmatrix} \otimes S_n, \\
\frac{\partial \Sigma_n(\theta)}{\partial \sigma_X^2 \partial \rho_{XY}} &= \begin{pmatrix} 0 & \frac{\sigma_Y}{2\sigma_X} \\ - & 0 \end{pmatrix} \otimes \Gamma_n, & \frac{\partial \Sigma_n(\theta)}{\partial \sigma_X^4} &= \begin{pmatrix} 0 & -\frac{\sigma_Y \rho_{XY}}{4\sigma_X^3} \\ - & 0 \end{pmatrix} \otimes \Gamma_n, \\
\frac{\partial \Sigma_n(\theta)}{\partial \sigma_Y^2 \partial b_{XY}} &= \begin{pmatrix} 0 & \frac{\sigma_X \rho_{XY}}{2\sigma_Y} \\ - & 1 \end{pmatrix} \otimes S_n, & \frac{\partial \Sigma_n(\theta)}{\partial \sigma_Y^2 \partial \rho_{XY}} &= \begin{pmatrix} 0 & \frac{\sigma_X}{2\sigma_Y} \\ - & 0 \end{pmatrix} \otimes \Gamma_n, \\
\frac{\partial \Sigma_n(\theta)}{\partial \sigma_Y^4} &= \begin{pmatrix} 0 & -\frac{\sigma_X \rho_{XY}}{4\sigma_Y^3} \\ - & 0 \end{pmatrix} \otimes \Gamma_n, & \frac{\partial \Sigma_n(\theta)}{\partial b_{XY} \partial \rho_{XY}} &= \begin{pmatrix} 0 & \sigma_X \sigma_Y \\ - & 0 \end{pmatrix} \otimes S_n, \\
\frac{\partial \Sigma_n(\theta)}{\partial b_{XY}^2} &= \begin{pmatrix} \sigma_X^2 & \sigma_X \sigma_Y \rho_{XY} \\ - & \sigma_Y^2 \end{pmatrix} \otimes SS_n, & \frac{\partial \Sigma_n(\theta)}{\partial \rho_{XY}^2} &= 0,
\end{aligned}$$

406 where $SS_n = \frac{\partial S_n}{\partial b_{XY}}$.

Because $\sup_n \lambda_{\max}\{\mathbf{0}\} < \infty$, the compact support of SS_n in b_{XY} , and the previous results, $\lambda_{\max}\{SS_n\} \leq \|SS_n\|_\infty < \infty$. Then, for $\sigma_X^2, \sigma_Y^2, \sigma_X \sigma_Y < \infty$,

$$\sup_n \lambda_{\max} \left\{ \frac{\partial^2 \Sigma_n(\theta)}{\partial b_{XY}^2} \right\} < \infty.$$

In addition,

$$\left\| \frac{\partial \Sigma_n(\theta)}{\partial \theta_i} \right\|_\infty \leq \left\| \frac{\partial \Sigma_n(\theta)}{\partial \theta_i} \right\| \leq \sqrt{n} \left\| \frac{\partial \Sigma_n(\theta)}{\partial \theta_i} \right\|_\infty.$$

407 This satisfies the first two conditions of Mardia and Marshall's theorem.

408 For the third condition, we consider $\mathbf{A} = [a_{ij}]_{i=j=1}^p$, with $a_{ij} = \left\{ \frac{t_{ij}}{(t_{mm} t_{nn})^{1/2}} \right\}$, and $t_{ij} =$
409 $\text{tr} \left\{ \Sigma_n(\theta)^{-1} \frac{\partial \Sigma_n(\theta)}{\partial \theta_i} \Sigma_n(\theta)^{-1} \frac{\partial \Sigma_n(\theta)}{\partial \theta_j} \right\}$ for all $i, j = 1, \dots, p$; we prove that \mathbf{A} is non singular.
410 Notice that

$$\mathbf{T} = [t_{ij}]_{i=j=1}^4 = \begin{pmatrix} \frac{n(\rho_{XY}^2 - 2)}{4\sigma_X^4(\rho_{XY}^2 - 1)} & \frac{n\rho_{XY}^2}{4\sigma_X^2\sigma_Y^2(\rho_{XY}^2 - 1)} & \frac{1}{2\sigma_X^2} \text{tr}\{\mathbf{A}_n\} & \frac{n\rho_{XY}}{2\sigma_X^2(\rho_{XY}^2 - 1)} \\ - & \frac{n(\rho_{XY}^2 - 2)}{4\sigma_Y^4(\rho_{XY}^2 - 1)} & \frac{1}{2\sigma_Y^2} \text{tr}\{\mathbf{A}_n\} & \frac{n\rho_{XY}}{2\sigma_Y^2(\rho_{XY}^2 - 1)} \\ - & - & \text{tr}\{[\mathbf{A}_n]^2\} & \frac{\rho_{XY}}{\rho_{XY}^2 - 1} \text{tr}\{\mathbf{A}_n\} \\ - & - & - & \frac{n(\rho_{XY}^2 + 1)}{(\rho_{XY}^2 - 1)^2} \end{pmatrix},$$

411 with $\mathbf{A}_n = \{\Gamma_n^{-1} \circ S_n\}$ where the operator \circ denotes the matrix Hadamard product.

412

Then,

$$\mathbf{A} = \begin{pmatrix} 1 & \frac{\rho_{XY}^2}{\rho_{XY}^2 - 2} & \frac{\text{tr}(\mathbf{A}_n)}{\left(\frac{n(\rho_{XY}^2 - 2)\text{tr}([\mathbf{A}_n]^2)}{\rho_{XY}^2 - 1} \right)^{1/2}} & \frac{\rho_{XY}}{\left(\frac{(\rho_{XY}^2 - 2)(\rho_{XY}^2 + 1)}{\rho_{XY}^2 - 1} \right)^{1/2}} \\ - & 1 & \frac{\text{tr}(\mathbf{A}_n)}{\left(\frac{n(\rho_{XY}^2 - 2)\text{tr}([\mathbf{A}_n]^2)}{\rho_{XY}^2 - 1} \right)^{1/2}} & \frac{\rho_{XY}}{\left(\frac{(\rho_{XY}^2 - 2)(\rho_{XY}^2 + 1)}{\rho_{XY}^2 - 1} \right)^{1/2}} \\ - & - & 1 & \frac{-\rho_{XY}\text{tr}(\mathbf{A}_n)}{(n\text{tr}([\mathbf{A}_n]^2)(\rho_{XY}^2 + 1))^{1/2}} \\ - & - & - & 1 \end{pmatrix}. \quad (\text{A.2})$$

413 For matrix \mathbf{A} in equation (A.2), we have extended the result established by Bevilacqua et al.
414 (2015). Thus \mathbf{A} is positive definite. By Mardia and Marshall's Theorem the ML estimator of
415 $\boldsymbol{\theta} = (\sigma_X^2, \sigma_Y^2, \rho_{XY}, b_{XY})^\top$ is asymptotically normal with variance $\mathbf{F}_n(\boldsymbol{\theta})^{-1}$.

416 Equation (10) implies that

$$\rho^c(\mathbf{h}) = g(\boldsymbol{\theta}) = \frac{2\rho_{XY}\sigma_X\sigma_Y \left(1 + (\nu + 1) \frac{\|\mathbf{h}\|}{b_{XY}} \right) \left(1 - \frac{\|\mathbf{h}\|}{b_{XY}} \right)_+^{\nu+1}}{\sigma_X^2 + \sigma_Y^2}.$$

Fixing $\nu > 0$, noting that $g(\cdot)$ is a continuously differentiable function for $\sigma_X \neq 0$ and $\sigma_Y \neq 0$, and using the multivariate delta method for $g(\cdot)$ we obtain

$$\left(\nabla g(\boldsymbol{\theta})^\top \mathbf{F}_n(\boldsymbol{\theta})^{-1} \nabla g(\boldsymbol{\theta}) \right)^{-1/2} (g(\boldsymbol{\theta}_n) - g(\boldsymbol{\theta})) \xrightarrow{D} N(0, 1),$$

where

$$\nabla g(\boldsymbol{\theta}) = \begin{pmatrix} \frac{\sigma_Y \rho_{XY} (\sigma_Y^2 - \sigma_X^2) \left(1 + (\nu + 1) \frac{\|\mathbf{h}\|}{b_{XY}} \right) \left(1 - \frac{\|\mathbf{h}\|}{b_{XY}} \right)_+^{\nu+1}}{\sigma_1 (\sigma_X^2 + \sigma_Y^2)^2} \\ \frac{\sigma_X \rho_{XY} (\sigma_X^2 - \sigma_Y^2) \left(1 + (\nu + 1) \frac{\|\mathbf{h}\|}{b_{XY}} \right) \left(1 - \frac{\|\mathbf{h}\|}{b_{XY}} \right)_+^{\nu+1}}{\sigma_Y (\sigma_X^2 + \sigma_Y^2)^2} \\ \frac{2\sigma_X \sigma_Y \left(1 + (\nu + 1) \frac{\|\mathbf{h}\|}{b_{XY}} \right) \left(1 - \frac{\|\mathbf{h}\|}{b_{XY}} \right)_+^{\nu+1}}{\sigma_X^2 + \sigma_Y^2} \\ \frac{2\sigma_X \sigma_Y \rho_{XY} f(b_{XY})}{\sigma_X^2 + \sigma_Y^2} \end{pmatrix},$$

$$f(b_{XY}) = \left(-\frac{(\nu + 1)\|\mathbf{h}\|}{b_{XY}^2} \right) \left(1 - \frac{\|\mathbf{h}\|}{b_{XY}} \right)_+^{\nu+1} + \left(1 + \frac{(\nu + 1)\|\mathbf{h}\|}{b_{XY}} \right) \left(1 - \frac{\|\mathbf{h}\|}{b_{XY}} \right)_+^\nu \frac{(\nu + 1)\|\mathbf{h}\|}{b_{XY}^2},$$

417

418

$$F_n^{-1}(\theta) = \begin{pmatrix} \frac{\sigma_X^4(n\text{tr}(\mathbf{B}^2) - C)}{nC} & \frac{\sigma_X^2\sigma_Y^2([\text{tr}(\mathbf{B})]^2 - 2\rho_{XY}^2C)}{nC} & -\frac{\sigma_X^2\text{tr}(\mathbf{B})}{C} & -\frac{\sigma_X^2\rho_{XY}(\rho_{XY}^2 - 1)}{n} \\ - & \frac{\sigma_Y^4(n\text{tr}(\mathbf{B}^2) - C)}{nC} & -\frac{\sigma_Y^2\text{tr}(\mathbf{B})}{C} & -\frac{\sigma_Y^2\rho_{XY}(\rho_{XY}^2 - 1)}{n} \\ - & - & \frac{C}{n} & 0 \\ - & - & - & \frac{(\rho_{XY}^2 - 1)^2}{n} \end{pmatrix},$$

⁴¹⁹ $\mathbf{B} = \left(\mathbf{R}^{-1} \frac{\partial \mathbf{R}}{\partial \phi} \right)$, $C = n\text{tr}(\mathbf{B}^2) - [\text{tr}(\mathbf{B})]^2$, and $\mathbf{R} = [R(\mathbf{h}, \phi)]_{i,j=1}^n$. □

420 References

421 References

- ⁴²² Anderes, E.B., Stein, M.L., 2011. Local likelihood estimation for nonstationary random fields. Journal of Multivariate Analysis 102, 506–520.
- ⁴²⁴ Atkinson, G., Nevill, A., 1997. Comments on the use of concordance correlation to assess the agreement between two variables. Biometrics 52, 775–778.
- ⁴²⁶ Barnhart, H.X., Haber, M.J., Line, L.I., 2007. An overview on assessing agreement with continuous measurements. Journal of Biopharmaceutical Statistics 17, 529–569.
- ⁴²⁸ Bevilacqua, M., Morales-Oñate, V., 2018. GeoModels: A Package for Geostatistical Gaussian and non Gaussian Data Analysis. URL: <https://vmoprojs.github.io/GeoModels-page/>. r package version 1.0.3-4.
- ⁴³¹ Bevilacqua, M., Faouzi, T., Furrer, R., Porcu, E., 2019. Estimation and prediction using generalized wendland covariance functions under fixed effects asymptotics. Annals of Statistics 47, 828–856.
- ⁴³⁴ Bevilacqua, M., Vallejos, R., Velandia, D., 2015. Assessing the significance of the correlation between the components of a bivariate gaussian random field. Environmetrics 26, 545–556.
- ⁴³⁶ Bustos, O., Ojeda, S., and, R.V., 2009. Spatial arma models and its applications to image filtering. Brazilian Journal of Probability and Statistics 23, 141–165.
- ⁴³⁸ Castillo-Páez, S., Fernández-Casal, R., García-Soidán, P., 2019. A nonparametric bootstrap method for spatial data. Computational Statistics and Data Analysis 137, 1–15.
- ⁴⁴⁰ Chodhary, P., Nagaraja, H., 2017. Measuring agreement, models, methods, and applications. Wiley, New York .
- ⁴⁴² Claverie, M., Ju, J., Masek, J.G., Dungan, J.L., Vermote, E. F. and Roger, J.C., Skakun, S.V., Justice, C., 2018. The harmonized landsat and sentinel-2 surface reflectance data set. Remote Sensing of Environment 219, 145–161.

- 445 Clayton, J., Modat, M., Presles, B., Anthopoulos, T., Daga, P., 2018. Package RNiftyReg.
446 URL: <https://cran.r-project.org/package=RNiftyReg>.
- 447 Cohen, J., 1968. Weighted kappa: Nominal scale agreement with provision for scale disagree-
448 ment or partial credit. *Psychological Bulletin* 70, 213–220.
- 449 Daley, D., Porcu, E., Bevilacqua, M., 2015. Classes of compactly supported covariance func-
450 tions for multivariate random fields. *Stochastic Environmental Research and Risk Assess-
451 ment* 29, 1249–1263.
- 452 Gao, F., Hilker, T., Zhu, X., Anderson, M., Masek, J., Wang, P., Yang, Y., 2015. Fusing landsat
453 and modis data for vegetation monitoring. *IEEE Geoscience and Remote Sensing Magazine*
454 3, 47–60.
- 455 Gillespie, A., Kahle, A., Walker, R., 1987. Color enhancement of highly correlated images. 2.
456 Channel ratio and chromaticity transformation techniques. *Remote Sensing of the Environ-
457 ment* 22, 343—365.
- 458 Gneiting, T., 2002. Compactly supported correlation functions. *Journal of Multivariate Anal-
459 ysis* 83, 493–508.
- 460 Gneiting, T., Kleiber, W., Schlather, M., 2010. Matérn cross-covariance functions for multi-
461 variate random fields. *Journal of the American Statistical Association* 105, 1167–1177.
- 462 Hiriote, S., Chinchilli, V.M., 2011. Matrix-based concordance correlation coefficient for re-
463 peated measures. *Biometrics* 67, 1007–1016.
- 464 Lawrence, I., Chinchilli, V., 1997. Rejoinder to the letter to the editor from atkinson and nevill.
- 465 Leal, C., Galea, M., Osorio, F., 2019. Assessment of local influence for the analysis of agree-
466 ment. *Biometrical Journal* 61, 955–972.
- 467 Lin, L., 1989. A concordance correlation coefficient to evaluate reproducibility. *Biometrics*
468 45, 255–268.
- 469 Lin, L., 2000. Total deviation index for measuring individual agreement: With application in
470 lab performance and bioequivalence. *Statistics and Medicine* 19, 255–270.
- 471 Lin, L., Hedayat, A., Sinha, B., Yang, M., 2002. Statistical methods in assessing agreement:
472 Models, issues, and tools. *Journal of the American Statistical association* 97, 257–270.
- 473 Lin, L., Hedayat, A.S., Wu, W., 2012. *Statistical Tools for Measuring Agreement*. Springer
474 Science & Business Media.
- 475 Makridakis, S., Taleb, N., 2009. “living in a world of low levels of predictability. *International
476 Journal of Forecasting* 25, 840–844.
- 477 Mardia, K.V., Marshall, T.J., 1984. Maximum likelihood estimation of models for residual
478 covariance in spatial regression. *Biometrika* 71, 135–146.

- 479 Mizunuma, T., Mencuccini, M., Wingate, L., Ogee, J., Nichol, C., et al., 2014. Sensitivity of
480 colour indices for discriminating leaf colours from digital photographs. Methods in Ecology
481 and Evolution 5, 1078–1085.
- 482 Nguy-Robertson, A.L., Buckley, E.M.B., Suyker, A.S., Awada, T.N., 2016. Determining fac-
483 tors that impact the calibration of consumer-grade digital cameras used for vegetation anal-
484 ysis. International Journal of Remote Sensing 37, 3365–3383.
- 485 Ojeda, S., Vallejos, R., Bustos, O., 2010. A new image segmentation algorithm with applica-
486 tions to image inpainting. Computational Statistics & Data Analysis 54, 2082–2093.
- 487 R Core Team, 2018. R: A Language and Environment for Statistical Computing. R Foundation
488 for Statistical Computing. Vienna, Austria. URL: <http://www.R-project.org/>.
- 489 Richardson, A.D., 2018. Tracking seasonal rhythms of plants in diverse ecosystems with digital
490 camera imagery. New Phytologist 00, <https://doi.org/10.1111/nph.15591>.
- 491 Schall, R., Williams, R.L., 1996. Towards a practical strategy for assessing individual bioe-
492 quivalence. Journal of Pharmacokinetics and Biopharmaceutics 24, 133–149.
- 493 Skiljan, I., 2014. IrfanView. URL: <https://www.irfanview.com/>.
- 494 Sonnentag, O., Hufkens, K., Teshera-Sterne, C., Young, A.M., Friedl, M., Braswell, B.H., Mil-
495 liman, T., O’Keefe, J., Richardson, A.D., 2012. Digital repeat photography for phenomenal
496 research in forest ecosystems. Agricultural and Forest Meteorology 152, 159–177.
- 497 Stevens, N.T., Steiner, S.H., MacKay, R.J., 2017. Assessing agreement between two measure-
498 ment systems: An alternative to the limits of agreement approach. Statistical Methods in
499 Medical Research 26, 2487–2504.
- 500 Toomey, M., Friedl, M.A., Frolking, S., Hufkens, K., Klosterman, S., et al., 2015. Green-
501 ness indices from digital cameras predict the timing and seasonal dynamics of canopy-scale
502 photosynthesis. Ecological Applications 25, 99–115.
- 503 Urbanek, S., 2014. Package jpeg. URL: <https://cran.r-project.org/package=jpeg>.
- 504 Vallejos, R., Mallea, A., Herrera, M., Ojeda, S., 2015. A multivariate geostatistical approach
505 for landscape classification from remotely sensed image data. Stochastic Environmental
506 Research and Risk Assessment 29, 369—378.
- 507 Vonesh, E.F., Chinchilli, V.M., Pu, K., 1996. Goodness of fit in generalized nonlinear mixed-
508 effect models. Biometrics 52, 572–587.
- 509 Wendland, H., 1995. Piecewise polynomial, positive definite and compactly supported radial
510 functions of minimal degree. Advances in computational Mathematics 4, 389–396.